ACCSCIENCE PUBLISHING

International Journal of Bioprinting

RESEARCH ARTICLE

3D-bioprinted kartogenin-laden hydrogel promotes cartilage regeneration via Smad1/5/9-mediated chondrogenesis of bone marrow stromal cells

Chenhui Yang[1,2,3], Changshun Chen[1,2], Rongjin Cheng[1,2], Fei Yang[1,2], Hefang Xiao[1,2], Bin Geng[1,2], and Yayi Xia[1,2]*

[1]Department of Orthopedics, Lanzhou University Second Hospital, Lanzhou, Gansu, China

[2]Department of Orthopedics I, Orthopedic Clinical Medical Research Center and Intelligent Orthopedic Industry Technology Center of Gansu Province, Lanzhou, Gansu, China

[3]Department of Orthopedics, Tianshui Hand and Foot Surgery Hospital, Tianshui, Gansu, China

Abstract

Cartilage injury and degeneration are common clinical problems that severely affect joint function and quality of life. Due to the limited self-healing capacity of cartilage, there is an urgent need for advanced biomaterials and strategies to promote effective cartilage regeneration. In this study, we present a 3D-bioprinted kartogenin (KGN)-loaded hydrogel with optimized biocompatibility and biomechanical properties for cartilage regeneration. By investigating the molecular mechanisms underlying KGN-induced chondrogenic differentiation of bone marrow stromal cells (BMSCs), we identified the critical role of the Smad1/5/9 signaling pathway through transcriptomic analysis. The hydrogel scaffold demonstrated uniform microstructure, robust mechanical stability, and controlled degradation, supporting BMSC adhesion and proliferation. *In vitro* experiments revealed that KGN activation of Smad1/5/9 significantly enhanced chondrogenic differentiation, evidenced by upregulated cartilage-specific matrix production and morphological changes in BMSCs, while pathway inhibition diminished this effect. Animal experiments using a rat model of cartilage injury demonstrated the hydrogel's biosafety, with no systemic toxicity or adverse inflammation, and its capacity to promote structured neocartilage formation rich in type II collagen. Histological and immunohistochemical analyses further validated the hydrogel's superior repair efficacy compared to controls. These findings highlight the dual functionality of the 3D-printed KGN-loaded hydrogel as a mechanically stable carrier and a bioactive inducer of BMSC chondrogenesis, mediated via Smad1/5/9 signaling, offering a promising strategy for cartilage tissue engineering.

Keywords: 3D bioprinting; Bone marrow stromal cells; Cartilage regeneration; Kartogenin; Smad1/5/9 pathway

***Corresponding author:**
Yayi Xia (xiayy@lzu.edu.cn)

Citation: Yang C, Chen C, Cheng R, *et al.* 3D-bioprinted kartogenin-laden hydrogel promotes cartilage regeneration via Smad1/5/9-mediated chondrogenesis of bone marrow stromal cells. *Int J Bioprint*. 2025;11(6):349-373. doi: 10.36922/IJB025180171

Received: April 28, 2025
Revised: July 29, 2025
Accepted: August 5, 2025
Published Online: August 5, 2025

1. Introduction

Cartilage injuries and degenerative joint diseases are common clinical disorders that significantly impact patients' quality of life. Given cartilage's limited intrinsic regenerative capacity, repair remains a significant challenge.[1] Treatment modalities, including pharmacotherapy and surgery, generally alleviate symptoms without fully regenerating the cartilage.[2,3] In recent years, 3D printing technology has emerged as an innovative manufacturing technique with substantial promise in biomedical applications, particularly tissue engineering.[4] This technology enables the precise construction of complex biological structures, offering novel solutions for cartilage tissue engineering by fabricating biomaterials with specific microstructures essential for supporting cell attachment, proliferation, and differentiation.[5,6]

With 3D printing, researchers have developed various hydrogels with excellent biocompatibility that mimic the natural cartilage environment. These hydrogels provide mechanical support and simulate the extracellular matrix (ECM), promoting cell growth and tissue regeneration.[7] Kartogenin (KGN), a small-molecule compound, has been demonstrated to induce bone marrow stromal cells (BMSCs) toward chondrogenic differentiation. Integrating KGN with 3D printing technology presents a new strategy for cartilage engineering.[8] Loading KGN into 3D-printed hydrogels creates a favorable microenvironment for BMSC chondrogenic differentiation, which has demonstrated potential in promoting cartilage regeneration in preliminary studies.[9]

The Smad1/5/9 signaling pathway is a key regulator in the differentiation process, particularly in the osteogenic and chondrogenic differentiation of BMSCs.[10,11] KGN influences this pathway to activate genes associated with cartilage formation.[12,13] Research on the Smad1/5/9 pathway enhances our understanding of BMSC differentiation mechanisms and provides a molecular basis for using these cells in tissue engineering.[14,15] By thoroughly investigating how this pathway regulates BMSC chondrogenic differentiation under the influence of KGN, we can more effectively design and optimize 3D-printed hydrogels to enhance their efficacy and safety in clinical applications.[16]

This study aims to develop a novel 3D-printed hydrogel material with excellent biocompatibility and mechanical properties, capable of effectively loading the small molecule compound KGN and significantly promoting chondrogenic differentiation of BMSCs by activating the Smad1/5/9 signaling pathway. By precisely designing the microstructure of the hydrogel and optimizing the release mechanism of KGN, this study not only validates its ability to promote chondrogenic differentiation of BMSCs *in vitro* but also evaluates its application in cartilage repair through animal models. This study introduces novel biomaterials and therapeutic approaches for managing cartilage lesions, with significant scientific and clinical implications. Especially in the context of limited existing treatment options, the 3D-printed hydrogel loaded with KGN (Hy@KGN) offers a more effective repair strategy for patients with cartilage damage, improving treatment outcomes and quality of life. Overall, the present study not only provides a new solution for chondrogenic differentiation but also lays the foundation for future clinical applications, with broad prospects and translational potential.

2. Materials and methods

2.1. Hydrogel synthesis

To synthesize Hy@KGN, hydroxyethyl methacrylate (HEMA; Sigma-Aldrich, United States of America [USA]) and poly(ethylene glycol) diacrylate (PEGDA; molecular weight [Mw]: 700, Sigma-Aldrich, USA) were dissolved in deionized water (Milli-Q, Merck Millipore, Germany). A solution containing 0.5 g of HEMA and 0.5 g of PEGDA in 5 mL of deionized water was stirred until completely dissolved. Subsequently, 0.05 g of ammonium persulfate (APS; Sigma-Aldrich, USA) and 0.05 mL of N,N,N′,N′-tetramethylethylenediamine (TEMED; Sigma-Aldrich, USA) were added and mixed thoroughly. Next, 0.05, 0.1, or 0.2 g of KGN (HY-16268, MedChemExpress, USA) was dissolved in 1 mL of ethanol and incorporated into the monomer solution, followed by uniform stirring. The mixture was printed into predesigned hydrogel structures using a 3D bioprinter (BioScaffolder 3.1, GeSiM, Germany) under the following parameters: printing temperature of 25°C; pressure of 30 psi; nozzle diameter of 0.203 mm; printing speed of 6 mm/s; and layer height of 0.2 mm.[17] After printing, the hydrogels were cured through chemical crosslinking to obtain the final Hy@KGN hydrogel. The hydrogel formulations are listed in **Table S1, Supporting Information**. The KGN release behavior was evaluated in a simulated body fluid environment. Release tests indicated that the hydrogel prepared with 0.2 g KGN released up to 85% of KGN within the first 2 weeks but exhibited higher cytotoxicity. In contrast, the hydrogel prepared with 0.1 g KGN released approximately 80% of KGN in the first 2 weeks with lower cytotoxicity and then entered a sustained release phase, providing a continuous supply of KGN to promote cartilage repair (Figure S1, Supporting Information). Based on these results, the hydrogel with 0.1 g KGN was selected for subsequent experiments.

2.2. Microstructure characterization

To examine the microstructure of the Hy@KGN hydrogel, scanning electron microscopy (SEM; FEI Quanta 250, Thermo Fisher Scientific, USA) was utilized. Firstly,

the printed hydrogel samples were freeze-dried for 48 h using a freeze dryer (Christ Alpha 1-2 LDplus, Martin Christ, Germany). Following dehydration, specimens were affixed to sample holders and subjected to gold sputter-coating. SEM imaging was performed at four distinct magnification levels to capture detailed structural features, and representative micrographs were recorded.

2.3. Rheological performance testing

To evaluate the viscoelastic behavior of the Hy@KGN hydrogel, a rheological analysis was performed using a rheometer (AR2000, TA Instruments, USA). Disc-shaped samples (diameter: 20 mm; thickness: 1 mm) were prepared for testing. Oscillatory frequency sweeps were carried out at 25°C over a range of 0.1–100 Hz under parallel plate configuration, and both storage modulus (G') and loss modulus (G'') values were recorded.

2.4. Compression performance testing

To measure the compressive properties of the Hy@KGN hydrogel, a compression tester (Instron 5567, Instron, USA) was utilized. Standard cylindrical hydrogel specimens (diameter: 10 mm; height: 10 mm) were prepared. Tests were conducted at room temperature at a compression speed of 1 mm/min. Compressive strength and maximum compressive strain were recorded, and a stress–strain curve was plotted.

2.5. Compression-reloading cycle testing

To evaluate the resilience and fatigue behavior of the Hy@KGN hydrogel, the same compression tester (Instron 5567, Instron, USA) was employed. Standard cylindrical hydrogel specimens (diameter: 10 mm; height: 10 mm) were placed between parallel compression plates of the tester. The tests were carried out at room temperature at a compression speed of 1 mm/min. After setting the maximum compressive strain, the tester initiated compression until the set strain was reached, followed by unloading. Force and displacement data were recorded throughout the process. The compression and unloading cycles were repeated multiple times (typically 10–20) to assess the hydrogel's resilience and fatigue behavior.

2.6. Tensile performance testing

The tensile properties of the Hy@KGN hydrogel were assessed using a tensile tester (Instron 5567, Instron, USA). Specimens were fabricated into standardized dumbbell configurations with dimensions of 75 mm (length), 4 mm (width), and 2 mm (thickness). Experiments were performed at ambient temperature under a constant extension rate of 10 mm/min. Key mechanical parameters, including ultimate tensile strength, fracture elongation, and elastic modulus, were measured, and corresponding stress–strain profiles were generated.

2.7. Water swelling experiment

To determine the water swelling capacity of the 3D-printed hydrogel, a hydration test was conducted. Initially, Hy@KGN hydrogel specimens (approximately 0.1 g in initial mass) were placed in an oven at 60°C until a constant weight was reached. After drying, the samples were immersed in deionized water and weighed hourly after gently removing surface water until equilibrium was reached (at least 30 h). The swelling ratio (SR) was calculated and plotted as:

$$SR = \frac{Wt - W0}{W0} \quad (I)$$

where W_t is the mass at time t and W_0 is the initial dry mass.

2.8. *In vitro* degradation experiment

To evaluate the *in vitro* degradation behavior of the 3D-printed hydrogel, degradation tests were performed. Hy@KGN hydrogel samples were cut into standard sizes (diameter: 10 mm; height: 2 mm) and immersed in phosphate-buffered saline (PBS) buffer (pH 7.4, Gibco, USA) at 37°C on a shaker set to 60 rpm. Samples were removed every 7 days over 8 weeks, dried of surface liquid, and weighed. The degradation rate was calculated and plotted as:

$$\text{Degradation rate} = \frac{W0 - Wt}{W0} \times 100\% \quad (II)$$

2.9. Adhesion strength test

The adhesion strength of the 3D-printed hydrogel in the cartilage repair region was measured using an Instron 5542 tester (Instron, USA). Hydrogel samples (diameter: 10 mm; height: 2 mm) were bonded to rat cartilage tissue (diameter: 10 mm) to create an adhesive interface. The bonded samples were incubated at 37 °C for 24 h to ensure full adhesion. Tensile tests were conducted at a speed of 1 mm/min, and the maximum force (F_{max}) and displacement were recorded. The adhesion strength (σ) was calculated as:

$$\sigma = \frac{Fmax}{A} \quad (III)$$

where A is the bonded area ($A = \pi \times (D/2)^2$; $D = 10$ mm). Each measurement was performed in triplicate to obtain the average adhesion strength.

2.10. Kartogenin release experiment

Release experiments were conducted to determine the release behavior of KGN from Hy@KGN hydrogels. Samples of Hy@KGN (diameter: 10 mm; height: 2 mm) were immersed in PBS buffer (pH 7.4, Gibco, USA) at 37°C on a shaker (60 rpm), with three replicates. Supernatant was collected at 24-h intervals for 14 consecutive days, with partial medium replacement using fresh PBS after each sampling. The KGN concentration in the collected solutions was determined via high-performance liquid chromatography (HPLC; Agilent 1260, Agilent Technologies, USA). The cumulative release was calculated as:

$$\text{Release} = \frac{\text{Ct} \times \text{V}}{m} \quad \text{(IV)}$$

where C_t is the concentration at time t, V is the total volume of the solution, and m is the initial sample mass. Thereafter, a KGN release curve was plotted.

2.11. RNA extraction

To evaluate the effect of KGN on BMSC gene expression, cells were divided into a control group (cultured in alpha minimum essential medium [α-MEM] supplemented with 10% fetal bovine serum [FBS]) and a KGN-treated group (α-MEM supplemented with 10% FBS and 10 μM KGN; Sigma-Aldrich, USA) for 48 h. Post-treatment, cells were harvested, washed with cold PBS, scraped, and centrifuged for RNA extraction.

RNA was extracted utilizing TRIzol reagent (Invitrogen, USA). Cells were thoroughly mixed with TRIzol, allowed to stand for 5 min to ensure complete cell lysis, followed by the addition of 200 μL chloroform (Sigma-Aldrich, USA), vigorous shaking, and phase separation by centrifugation at 12,000 × *g* for 15 min at 4°C. The aqueous phase was mixed with 500 μL isopropanol (Sigma-Aldrich, USA) to precipitate RNAs, then washed twice with 75% ethanol, and dissolved in RNase-free water. RNA concentration and purity were determined using NanoDrop 2000 (Thermo Fisher Scientific, USA), with acceptable A260/A280 ratios between 1.8 and 2.0. RNA integrity was verified using an Agilent 2100 Bioanalyzer (Agilent Technologies, USA), and samples with RNA integrity number (RIN) ≥7.0 were used for further analysis.

2.12. RNA-sequencing analysis

RNA samples were sequenced using the Illumina HiSeq platform. Initially, RNA libraries were prepared using the TruSeq RNA Sample Preparation Kit (Illumina, USA). Once library construction was completed, the quality of the libraries was assessed using the Agilent 2100 Bioanalyzer. Qualified library samples were then sequenced on the Illumina HiSeq 2500 system, generating approximately 50–60 million reads per sample, with a read length of 150 bp. Upon completion of sequencing, raw reads were obtained for subsequent quality control and bioinformatics analysis.

2.13. Data processing and quality control

The raw sequencing data generated by the Illumina HiSeq platform were subjected to quality control and filtering. FastQC was employed to evaluate data quality, and sequences with poor quality or adapter contamination were removed to retain only high-confidence reads for downstream analysis. The reads were then aligned to the reference genome using STAR, utilizing the latest version released by Ensembl. Finally, transcriptome assembly and quantification were performed using StringTie, with gene expression levels reported as FPKM (Fragments Per Kilobase of transcript per Million mapped reads).

2.14. Differentially expressed gene analysis

Differentially expressed gene (DEG) analysis between the control and KGN-treated groups was performed using the DESeq2 or EdgeR package. Genes with $|\log_2\text{FoldChange}| > 1$ and p-values < 0.05 were considered significant DEGs. Volcano plots and heatmaps were generated to visualize the expression patterns and significance of the DEGs.

2.15. Functional enrichment analysis

Enrichment analysis was conducted to evaluate the functional roles of DEGs in terms of biological processes, cellular structures, and molecular activities. The ClusterProfiler tool was employed to perform Gene Ontology (GO) and KEGG pathway analyses, applying a significance threshold of adjusted p-value < 0.05. Particular focus was placed on genes associated with chondrogenic differentiation and the Smad1/5/9 signaling cascade. The top enriched GO terms and KEGG pathways were illustrated using bar plots.

2.16. Weighted gene co-expression network analysis

Weighted gene co-expression network analysis (WGCNA) was constructed to identify gene modules associated with specific phenotypes. Initially, gene expression matrices were loaded using the WGCNA package. Data preprocessing included sample clustering, outlier detection, and normalization. An appropriate soft threshold (power) ensures a scale-free network topology. A weighted gene co-expression network was built by calculating gene similarities, which were then transformed into an adjacency matrix and further into a Topological Overlap Matrix (TOM). Genes were clustered into modules using dynamic tree cutting, and a heatmap illustrating module-trait relationships was created to identify key modules

significantly associated with KGN treatment and explore their biological functions. Genes from these key modules were further analyzed.

2.17. Protein–protein interaction network analysis

Protein–protein interaction (PPI) analysis was conducted to investigate interactions among proteins and identify critical regulatory elements. Interaction data were retrieved from the STRING database (v11.0, https://string-db.org/), using gene sets from selected modules and specifying the relevant species (e.g., human or rat) with a minimum interaction confidence score of 0.4. The interaction networks were constructed and visualized in Cytoscape (v3.7.2). Hub genes were identified using five algorithms integrated via the CytoHubba plugin.

2.18. Cell isolation and culture

Bone marrow stromal cells (BMSCs) were obtained from male Sprague-Dawley rats (6–8 weeks old; Beijing Vital River Laboratory Animal Technology Co., Ltd., China). Bone marrow was collected and cultured in Dulbecco's Modified Eagle Medium (DMEM; Gibco, USA) enriched with 10% FBS and 1% penicillin–streptomycin. Cells were maintained at 37°C in a 5% CO_2 incubator. Morphology and flow cytometry were used to characterize BMSCs.

Articular chondrocytes were isolated from the knees of 4-week-old Sprague-Dawley rats and seeded into 96-well plates at 5000 cells/well in DMEM/F12 medium containing 10% FBS, 100 mg/mL streptomycin, and 100 U/mL penicillin. For NF-κB translocation assays, chondrocytes were stimulated with 10 ng/mL IL-1β.

2.19. Flow cytometry

Flow cytometric analysis was performed using a Fortessa flow cytometer (BD Biosciences, USA) to assess BMSC markers. After PBS washing, cells were incubated with fluorochrome-conjugated antibodies against CD44, CD90, CD105, CD73, CD146, CD45, CD34, and HLA-DR (Miltenyi Biotec, USA), along with corresponding isotype controls. Stained cells were incubated on ice for 30 min, washed with MACS buffer (Miltenyi Biotec, USA), and resuspended in the same buffer for analysis. Cell surface marker expression was analyzed using FlowJo software (TreeStar, USA).

2.20. Cell grouping

Bone marrow stromal cells (BMSCs) and chondrocytes were randomly assigned into the following four experimental groups: the control group (PBS treatment), a hydrogel-only group (3D-printed hydrogel lacking KGN), a KGN group (treated with 10 μM KGN in DMEM), and a Hy@KGN group (cultured with leachate from Hy@KGN hydrogels). All cell groups were seeded into 6-well plates at a density of 5×10^4 cells per well.

2.21. Cell Counting Kit-8 (CCK-8) assay

The cytotoxicity of Hy@KGN on BMSCs was evaluated using the Cell Counting Kit-8 (CCK-8; Dojindo, Japan). BMSCs were seeded in 96-well plates at 1.2×10^4 cells per well across four treatment groups. After 24 h, the medium was removed and replaced with 100 μL of fresh medium containing 10 μL of CCK-8 reagent. Following a 4-h incubation at 37 °C, absorbance at 450 nm was measured using a microplate reader (BioTek, USA). Cell viability was determined by subtracting background values and normalizing to the untreated control.

2.22. Live/dead fluorescence staining

The viability of BMSCs was assessed using the Live/Dead Cell Vitality/Toxicity Assay Kit (Invitrogen, USA). According to the grouping scheme, cells were plated in 24-well plates and incubated for 24 h. Afterward, they were stained in the dark with a solution containing 1 mM calcein-AM and 2 mM ethidium homodimer-1 (EthD-1). Live cells (green) and dead cells (red) were visualized using an inverted fluorescence microscope (IX73, Olympus, Japan). The proportion of viable cells was quantified using ImageJ software.

2.23. Induction of chondrogenic differentiation and staining

For cell culture, BMSCs were seeded directly onto the 3D-printed hydrogel scaffolds in 24-well plates at 6×10^4 cells per well and cultured for 2 days in low-glucose DMEM supplemented with 10% inactivated FBS, 100 U/mL penicillin, and 100 μg/mL streptomycin. From the third day, chondrogenic differentiation was induced using a chondrogenic medium (Cat. A1007101, ThermoFisher, USA) for 3 weeks. After cultivation, the medium was aspirated, and cells were fixed in 10% neutral buffered formalin for 24 h. Samples underwent a graded dehydration process in 50%, 70%, 90%, and 100% ethanol, each for 15 min, followed by two 15-min clearings in xylene. The clarified cells were then embedded in paraffin, sectioned to 5 μm thickness, and rehydrated through 100%, 90%, 70%, and 50% ethanol and distilled water, each for 5 min. The sections were stained with toluidine blue, hematoxylin and eosin (H&E), and Alcian blue. For toluidine blue, sections were stained in 0.1% toluidine blue solution (Sigma-Aldrich, USA) for 10 min and washed three times with distilled water. For H&E staining, sections were stained with hematoxylin for 5 min, rinsed until clear, and then stained with eosin for 3 min. For Alcian blue staining, sections were stained in 1% Alcian blue solution (pH 2.5, Sigma-Aldrich, USA) for 30 min and washed three times. Stained sections were observed and photographed utilizing a microscope (Olympus, Japan).

2.24. Western blot

To detect the expression of proteins associated with chondrogenic differentiation, total proteins were extracted from BMSCs and rat femur tissues using RIPA buffer containing protease inhibitors. Equal amounts of protein were separated via 10% SDS-PAGE and transferred onto PVDF membranes (Millipore, USA). The membranes were blocked with 3% bovine serum albumin (BSA) to minimize non-specific binding, followed by overnight incubation at 4°C with primary antibodies targeting COL2A1 (Cat. no. ab34712, 1:1000, Abcam, USA), ACAN (Cat. no. ab315486, 1:1000, Abcam, USA), SOX9 (Cat. no. ab185966, 1:1000, Abcam, USA), PRG4 (Cat. no. ab28484, 1:1000, Abcam, USA), COX-2 (Cat. no. ab179800, 1:1000, Abcam, USA), matrix metalloproteinase (MMP)-3 (Cat. no. ab52915, 1:1000, Abcam, USA), p65 (Cat. no. ab76302, 1:1000, Abcam, USA), Smad1/5/9 (Cat. no. ab92698, 1:1000, Abcam, USA), phospho-Smad1/5/9 (Cat. no. ab300164, 1:1000, Abcam, USA), and β-actin (A5441, 1:5000, Sigma-Aldrich, USA) as a loading control. Following TBST washing, membranes were incubated with horseradish peroxidase (HRP)-conjugated secondary antibodies and visualized using an enhanced chemiluminescence (ECL) detection kit (Thermo Fisher Scientific, USA). Chemiluminescent signals were captured with an ImageQuant LAS4000mini system (Sweden). Densitometric analysis was conducted using Gel-Pro Analyzer (Media Cybernetics, USA) to quantify protein levels associated with chondrogenesis and Smad pathway activation.

2.25. Reverse transcription quantitative polymerase chain reaction

Reverse transcription quantitative polymerase chain reaction (RT-qPCR) was performed to evaluate the expression of chondrogenesis-related genes. Total RNA was extracted from each group of BMSCs utilizing Trizol reagent (Invitrogen, USA). The purity and concentration of the extracted RNA were determined using NanoDrop 2000 (Thermo Fisher Scientific, USA), and RNA integrity was assessed by 1% agarose gel electrophoresis. Subsequently, 1 μg of total RNA was reverse-transcribed into complementary DNA (cDNA) using the PrimeScript RT kit (Takara, Japan). RT-qPCR reactions were carried out using SYBR Green PCR Master Mix (Applied Biosystems, USA) in a 20 μL total volume, containing 10 μL of master mix, 0.4 μL each of 10 μM forward and reverse primers, 1 μL cDNA, and 8.2 μL nuclease-free water. Amplification was performed on an ABI 7500 Real-Time PCR System (Applied Biosystems, USA) under the following conditions: 95 °C for 10 min, followed by 40 cycles of 95 °C for 15 s and 60 °C for 1 min. All samples were analyzed in triplicate, with β-actin serving as an internal control. Relative gene expression was quantified utilizing the $2^{-\Delta\Delta Ct}$ method. Primer sequences are listed in Table S2, Supporting Information.

2.26. Phalloidin staining

To observe cytoskeletal changes in BMSCs, phalloidin staining was performed. BMSCs were divided into four groups per experimental design and seeded in 6-well plates at a density of 4×10^5 cells per well. After incubation, cells were fixed with 4% paraformaldehyde (PFA; Sigma-Aldrich, USA) for 15 min, then rinsed three times with PBS (5 min each). Permeabilization was performed using 0.1% Triton X-100 for 10 min at room temperature. After additional PBS washes, cells were incubated with phalloidin staining solution (Sigma-Aldrich, USA) at 37 °C for 30 min, followed by three PBS rinses. Cytoskeletal morphology was imaged using a fluorescence microscope (IX73, Olympus, Japan).

2.27. Immunofluorescence staining

NF-κB nuclear translocation in chondrocytes was assessed via immunofluorescence. BMSCs were plated in 6-well plates at 4×10^5 cells/well and treated according to experimental grouping. After 3 h of incubation and stimulation, cells were fixed with 4% PFA for 1 h, washed with PBS, and permeabilized using 0.1% Triton X-100 for 30 min. Non-specific binding was blocked with 1% BSA for 1 h at room temperature. Cells were then incubated with NF-κB p65 primary antibody (1:500; Santa Cruz Biotechnology, USA) for 1 h, followed by three PBS + 0.1% Tween-20 washes and subsequent incubation with FITC-conjugated secondary antibody (Invitrogen, USA) for 1 h. Nuclear staining was performed with DAPI (Sigma-Aldrich, USA) for 5 min. After the final PBS washes, cells were mounted in 50% glycerol and examined using a fluorescence microscope (IX73, Olympus, Japan).

2.28. Establishment of the rat cartilage defect model

Twelve-week-old male Sprague-Dawley rats (400–450 g; Cat. no. 101, Beijing Vital River Laboratory Animal Technology Co., Ltd., China) were housed individually in an specific pathogen-free (SPF) animal laboratory with controlled humidity (60–65%), temperature (22–25°C), and a 12-h light/dark cycle, with free access to food and water. Following a 7-day acclimatization period and baseline health monitoring, all procedures were approved by the Institutional Animal Care and Use Committee (Approval no. D2025-365) and conducted in accordance with institutional animal care guidelines.

Rats were randomly assigned to the following five groups: the PBS control group (injection of PBS into the osteochondral defect area as a baseline comparison), the Hy hydrogel group (implantation of a 3D-printed hydrogel without any drug into the defect area), the KGN

administration group (direct injection of KGN into the defect area), the Hy@KGN group (implantation of a Hy@KGN into the defect area), and the LDN+Hy@KGN group (implantation of Hy@KGN into the defect area and injection of the Smad1/5/9 pathway inhibitor LDN-193189). The dosage of LDN-193189 (Cat. no. S2618, Selleck, China) was 3 mg/kg, and the dosage of KGN (Cat. no. S7658, Selleck, China) was 5 mg/kg.[18–21]

Under 2–4% isoflurane anesthesia, rats were prepped aseptically, and a medial patellar incision exposed the femoral trochlea. A cylindrical full-thickness cartilage defect (1.5 mm diameter × 2 mm depth) was created using a custom drill, and treatment materials were applied according to group allocation. The surgical site was irrigated with sterile saline, closed, and treated with postoperative antibiotics (Baytril, Bayer, Germany). At 6 and 12 weeks post-operation, rats were euthanized using pentobarbital, and distal femurs were harvested for gross evaluation using the International Cartilage Repair Society (ICRS) scoring system.[16,19,22]

Post-surgery, the rats' body weight and behavioral changes were regularly monitored. The rats were weighed weekly using an electronic scale (Sartorius, Germany), and food and water intake were recorded. The activity levels and pain responses of the rats were also observed.

2.29. Biosafety evaluation

To assess the biosafety of the 3D-printed hydrogel, healthy adult Sprague-Dawley rats were selected, and subcutaneous implantation surgery was performed under sterile conditions. Anesthesia was induced using isoflurane (Baxter, USA), and a small incision was made on the dorsal skin of the rats to implant a 1 cm^3 3D-printed hydrogel. The incision was sutured using silk sutures (Ethicon, USA). Rats were randomly divided into three groups: the control group (no experimental procedures performed, serving as baseline), the sham group (underwent all surgical steps but without hydrogel implantation), and the hydrogel implantation group (subcutaneous implantation of Hy@KGN). Each group consisted of 10 rats.

Blood samples were collected weekly from the tail vein, and complete blood counts were conducted using an automated hematology analyzer (Sysmex, Japan). Serum biochemical markers, including ALT, AST, BUN, and creatinine, were assessed using a chemiluminescence immunoassay system (Roche, Switzerland) to monitor liver and kidney function.

At study completion, rats were euthanized, and major organs (heart, liver, spleen, lung, kidney) were harvested, fixed in 4% formaldehyde (Sigma-Aldrich, USA), embedded, sectioned, and stained with H&E. Histopathological examination was performed under an optical microscope (Olympus, Japan) to assess tissue morphology and potential toxicity.

2.30. TUNEL staining

Apoptotic cells were detected using a TUNEL assay kit (Cat. no. C1086, Beyotime, China). Paraffin-embedded tissue sections were processed and stained, and TUNEL-positive cells displaying green fluorescence were visualized under a fluorescence microscope (IX73, Olympus, Japan). Six random fields per section were selected for quantification using ImageJ software.

2.31. ELISA for inflammatory cytokine detection

Serum levels of inflammatory cytokines IL-6 (R6000B), TNF-α (RTA00), and IL-1β (RLB00) were measured using ELISA kits (R&D Systems, USA) to evaluate the systemic inflammatory response. Absorbance was measured using a microplate reader (BioTek, USA), and cytokine concentrations were calculated based on standard curves.

2.32. Histological examination

In this experiment, femurs were initially harvested from exposed joint cavities and fixed in 4% PFA for 48 h. Following fixation, the osteochondral specimens underwent micro-computed tomography (micro-CT) to capture structural details. The specimens were then decalcified in 10% ethylenediaminetetraacetic acid (EDTA) solution for 4 weeks, with daily solution changes. After decalcification, samples were bisected longitudinally through the center of the defect, embedded in paraffin, and sectioned at 5 μm thickness. Sections were deparaffinized, rehydrated, and stained with H&E, Safranin O/Fast Green (SO/FG), Alcian Blue, and Sirius Red. Morphological features of cartilage and subchondral bone were examined under a Leica microscope (Leica Microsystems, Germany), and cartilage repair was graded based on the ICRS visual histological scoring criteria.

2.33. Immunohistochemical analysis

The expression of Bcl-2, collagen I, and collagen II was detected using the streptavidin-biotin peroxidase complex method. Initially, paraffin-embedded sections were processed through standard dewaxing, hydration, and heat-induced antigen retrieval in citrate buffer (pH 6.0). The sections were then blocked with 10% horse serum to prevent non-specific binding and incubated with an endogenous peroxidase blocker for 10 min. Primary antibodies were applied: Bcl-2 (Cat. no. ab196495, 1:250, Abcam, USA), collagen I (Cat. no. ab270993, 1:100, Abcam, USA), and collagen II (Cat. no. ab34712, 1:200, Abcam, USA), and incubated overnight at 4°C. Following PBS washing, HRP-conjugated goat anti-rabbit secondary antibody (Cat. no. ab6721, 1:500, Abcam, USA) was

applied at 37°C for 30 min, followed by streptavidin-biotin incubation and DAB color development. Nuclei were counterstained with hematoxylin. Stained sections were visualized under a light microscope, and ImageJ software was used for quantitative analysis of Bcl-2-positive cells and the area fraction of collagen I/II.

2.34. Micro-computed tomography analysis

Micro-computed tomography (micro-CT) was employed to assess subchondral bone regeneration at defect sites (n = 10 per group) using the SkyScan 1272 system (Bruker, Belgium). Scans were conducted with a voltage of 70 kV, current of 112 μA, 0.2 mm aluminum filter, and 18 μm voxel resolution. 3D reconstructions were generated using CTVol software. Mineralized bone was identified using a threshold of 1400, and key parameters, including bone volume fraction (BV/TV), bone defect volume ratio (BDV/TV), bone mineral density (BMD), and trabecular separation (Tb.Sp), were quantified to evaluate the extent of bone repair.

2.35. Masson's trichrome staining

Masson's trichrome staining was performed to examine collagen deposition in the cartilage repair areas of experimental rats. Corresponding tissue sections were dewaxed, rehydrated, and stained utilizing a Masson's trichrome staining kit (Sigma-Aldrich, USA). This staining method distinguishes collagen fibers (blue), muscle fibers (red), and nuclei (black). Images were captured using a microscope to quantitatively analyze the distribution and density of collagen fibers.

2.36. Statistical analysis

All statistical analyses were carried out using GraphPad Prism 9.5.0 (GraphPad Software, Inc., USA) and R version 4.2.1 (R Foundation for Statistical Computing, Austria). Quantitative data are expressed as mean ± standard deviation. For comparisons between two groups, independent samples t-tests were used after confirming normality with the Shapiro–Wilk test. For comparisons among multiple groups, one-way analysis of variance (ANOVA) was conducted with Tukey's post-hoc test, and normality was also assessed prior to ANOVA. If data did not meet normality assumptions, non-parametric tests (e.g., Kruskal–Wallis test) were applied instead. A p-value < 0.05 was considered statistically significant.

3. Results

3.1. Kartogenin activation of the Smad1/5/9 signaling pathway enhances chondrogenic differentiation of BMSCs

In this study, we successfully isolated and cultured rat BMSCs and conducted a comprehensive characterization. Morphological observations and flow cytometry analysis confirmed that the isolated BMSCs exhibited typical stem cell-like morphology (Figure S2A, Supporting Information). Flow cytometry results indicated high expression levels of markers CD44, CD90, CD105, CD73, and CD146 in BMSCs, while positive expression rates for CD45, CD34, and HLA-DR were below 2% (Figure S2B, Supporting Information). Subsequently, BMSCs were treated with KGN, and gene expression changes before and after treatment were analyzed using RNA-sequencing (RNA-seq), yielding high-quality sequencing data (Figure 1A). Approximately, 50 million 150 bp reads per sample were generated, with data quality control performed using FastQC, revealing that all samples had a Q30 score above 95%. High-quality reads were aligned to the reference genome with an average alignment rate exceeding 90%. Differential expression analysis identified 1223 significantly DEGs, with 569 upregulated and 654 downregulated (Figure 1B and C).

Gene Ontology (GO) and KEGG enrichment analyses revealed that DEGs were involved in biological processes such as cytoskeletal reorganization, ECM binding, cell migration, and proliferation (Figure S3A, Supporting Information). Notably, KEGG pathway analysis revealed marked upregulation in the TGF-β and Wnt signaling pathways, as well as ECM receptor interactions, in the KGN-treated group (Figure S3B and C, Supporting Information). Moreover, expression levels of key genes such as *Acan*, *Bmp2*, *Bmp6*, *Smad1*, *Smad5*, and *Smad9* were significantly increased (Figure 1D). These findings suggest that KGN treatment activates critical signaling pathways associated with chondrogenic differentiation in BMSCs.

Weighted gene co-expression network analysis (WGCNA) further elucidated gene modules associated with KGN treatment. Analysis of the scale-free fit index and the average connectivity identified an appropriate soft-thresholding power. At a soft-thresholding power of 5, the scale-free fit index reached 0.85, and average connectivity remained within a reasonable range (Figure S4A, Supporting Information). The clustering of DEG modules produced a dendrogram that illustrated the clustering relationships among the modules (Figure S4B, Supporting Information). The correlation heatmap revealed that the gene module colored in antiquewhite1 exhibited the highest correlation with the KGN treatment group (r = 0.99, $p < 0.01$) (Figure 1E). Specifically, the antiquewhite1 module included several known regulators of chondrogenic differentiation, such as *Sox9*, *Col2a1*, and *Tgfbr1*, each with correlation coefficients exceeding 0.9 (Figure 1F). KEGG pathway analysis indicated that this module was predominantly

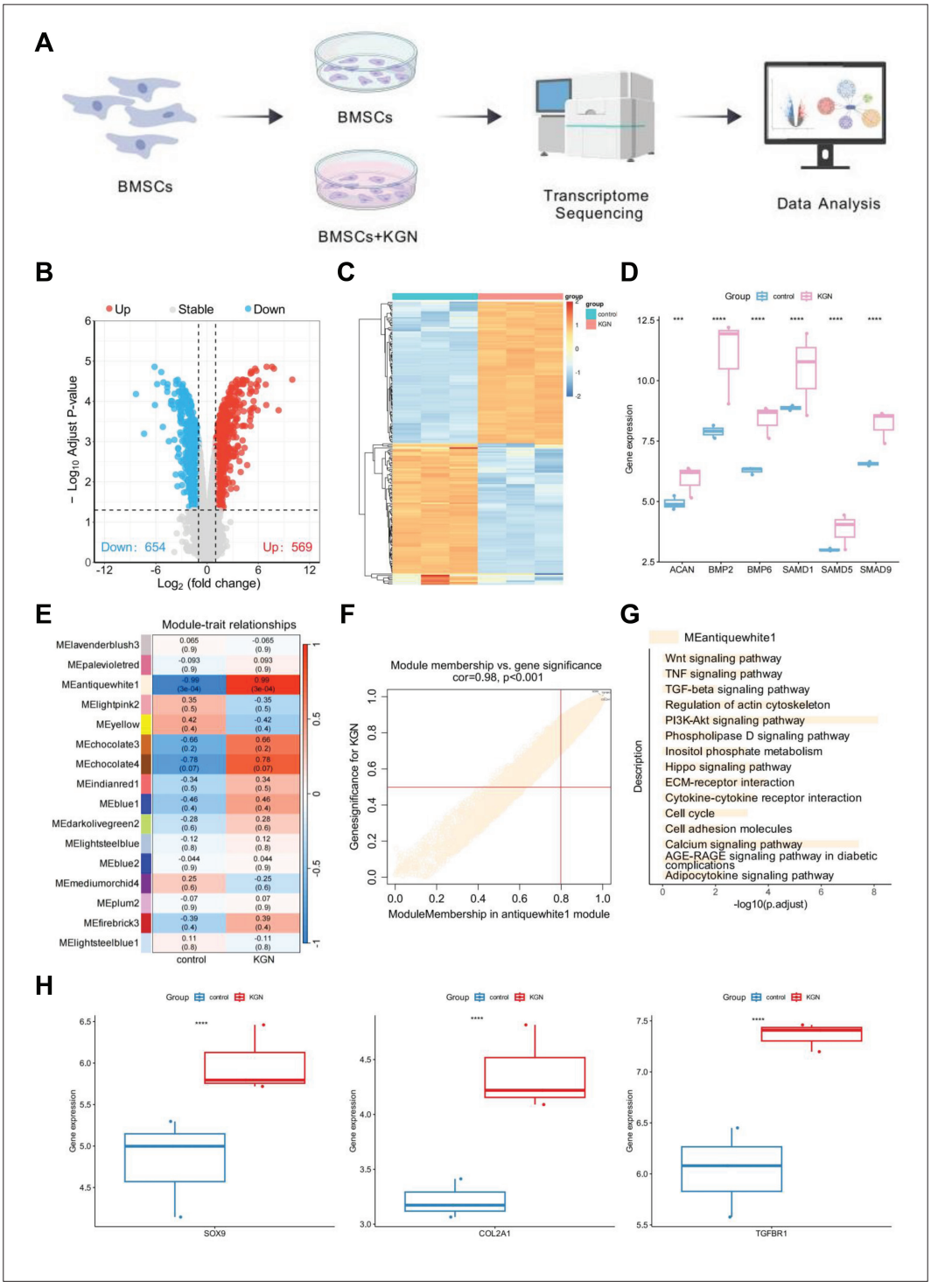

Figure 1. Differential gene expression analysis and screening of chondrogenic differentiation-related genes in BMSCs after KGN treatment. (A) RNA-sequencing analysis workflow. (B) Volcano plot displaying DEGs between the KGN-treated and control groups, with upregulated genes in red and downregulated genes in blue. (C) Heatmap of DEGs between the KGN-treated and control groups. (D) Expression levels of *Acan*, *Bmp2*, *Bmp6*, *Smad1*, *Smad5*, and *Smad9* in the KGN-treated versus control groups. (E) Correlation heatmap between each module and both the control and KGN-treated groups, with each cell displaying the correlation coefficient and *p*-value. (F) Significance analysis of the antiquewhite1 module in the KGN-treated group, with each point representing a gene. (G) KEGG enrichment analysis of the antiquewhite1 module. (H) Box plot of significant chondrogenic differentiation-related genes in the antiquewhite1 module, displaying high expression of *SOX9*, *COL2A1*, and *TGFBR1* in the KGN-treated group. * denotes significance between groups, ***$p < 0.001$, ****$p < 0.0001$. Abbreviations: BMSCs: bone marrow stromal cells; DEGs: differentially expressed genes; KGN: kartogenin.

associated with chondrogenic differentiation, involving pathways like TGF-β, Wnt signaling, and regulation of the actin cytoskeleton (Figure 1G). Expression box plots demonstrated that genes related to chondrogenic differentiation were highly expressed in the KGN treatment group, particularly noting significant increases in *Sox9, Col2a1*, and *Tgfbr1* (Figure 1H).

Furthermore, we constructed a PPI network for the key gene modules in the KGN treatment group using the STRING database to explore core regulatory factors (Figure 2A). Analysis revealed that Smad1, Smad5, and Smad9 had high degrees of connectivity within the network, indicating their pivotal roles in chondrogenic differentiation. The MCODE plugin identified four sub-modules related to chondrogenic differentiation, further confirming the importance of Smad1, Smad5, and Smad9 within these sub-modules (Figure 2B). The network also detailed interactions among other significant chondrogenic differentiation regulatory genes, unveiling their synergistic actions in KGN-induced chondrogenic differentiation (Figure 2C). Using the cytohubba plugin, we identified key nodes within the chondrogenic differentiation network

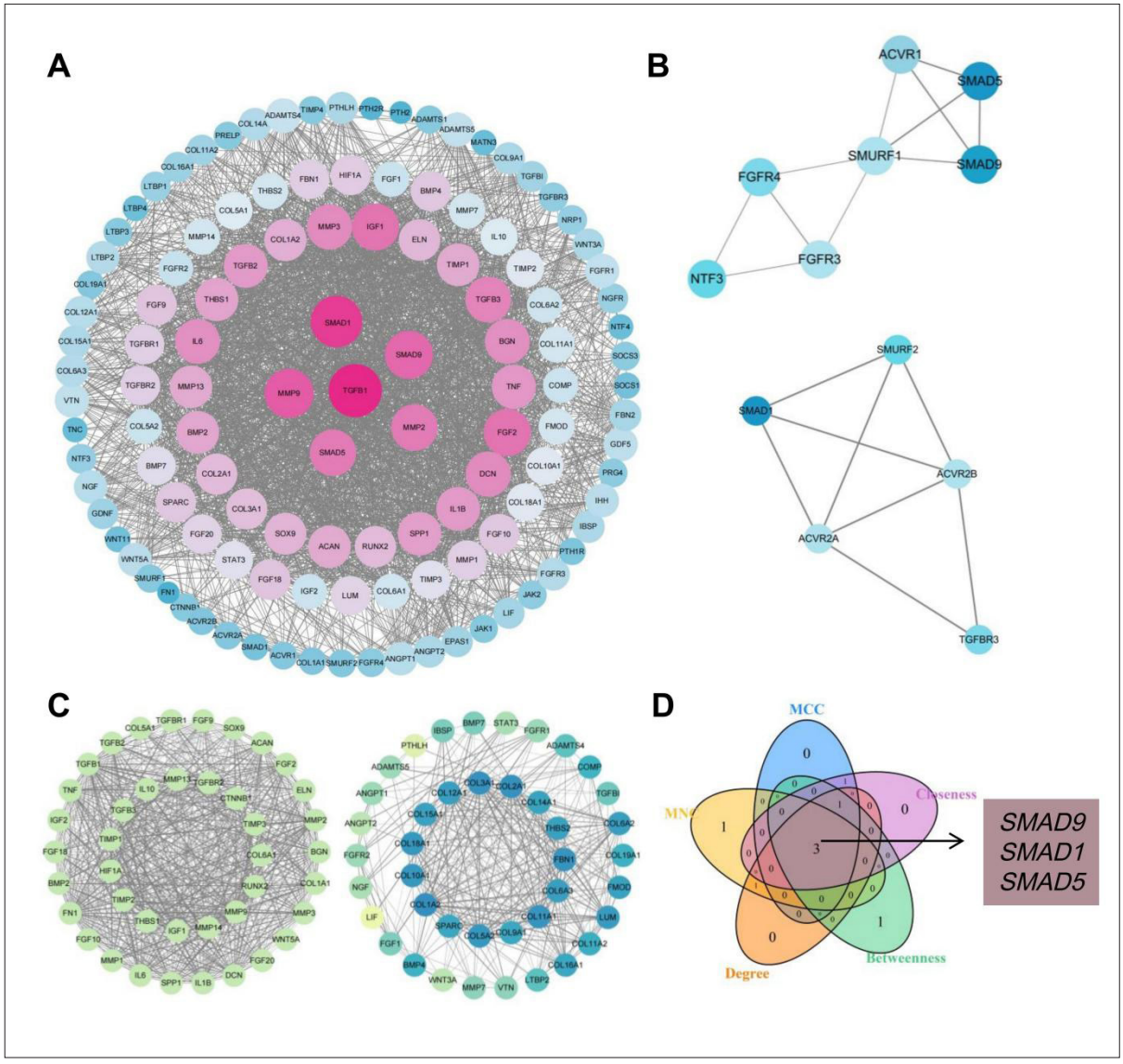

Figure 2. Protein–protein interaction (PPI) network analysis reveals key regulatory factors. (A) PPI network of chondrogenic differentiation-related module genes in the kartogenin (KGN)-treated group, with node degrees represented by a gradient from pink to blue. (B) Interaction relationships of genes, including *Smad1*, *Smad5*, and *Smad9*, in the MCODE module. (C) Interaction relationships of other significant chondrogenic regulatory genes in the MCODE module. (D) Venn diagram displaying three critical chondrogenic differentiation-related genes identified through five cytohubba methods.

Table 1. Cytohubba plugin selects key genes based on five metrics

Metric	Genes				
MCC	MMP9	SMAD9	MMP2	SMAD1	SMAD5
MNC	TGFB1	COL1A1	SMAD9	SMAD1	SMAD5
Degree	TGFB1	MMP9	SMAD9	SMAD1	SMAD5
Betweenness	SMAD9	MMP9	SMAD5	SMAD1	ACAN
Closeness	MMP9	SMAD9	MMP2	SMAD1	SMAD5

Abbreviations: ACAN, aggrecan; COL1A1, collagen type I alpha 1 chain; MCC, maximal clique centrality; MMP, matrix metalloproteinase; MNC, maximum neighborhood component;; SMAD, mothers against decapentaplegic homolog; TGFB1, transforming growth factor beta 1.

(Table 1). By integrating results from five analytical methods, we pinpointed three crucial regulatory factors: Smad9, Smad1, and Smad5 (Figure 2D). These findings further support the central role of Smad1, Smad5, and Smad9 in chondrogenic differentiation.

These results demonstrate that KGN treatment activates the Smad1/5/9 signaling pathway, thereby promoting chondrogenic differentiation in BMSCs.

3.2. Preparation and characterization of Hy@KGN

We successfully synthesized a 3D-printed hydrogel material, Hy@KGN, with excellent biocompatibility and mechanical properties by incorporating the small molecule compound KGN into the hydrogel matrix (Figure 3A). The visible light image of the Hy@KGN hydrogel is presented in Figure 3B. SEM at various magnifications revealed a uniform distribution of micropores within the hydrogel, with pore diameters of 50–100 μm that supported cell adhesion and proliferation (Figure 3C). Additionally, the disc-shaped Hy@KGN hydrogel produced via 3D printing demonstrated good stability with no signs of brittleness, such as cracks or defects, making it suitable for cartilage repair and drug delivery (Figure 3D). Rheological measurements demonstrated that the *G*' of Hy@KGN was 500 Pa, and the *G*" was 200 Pa, indicating desirable elastic and viscoelastic properties (Figure 3E). Compression tests revealed that Hy@KGN hydrogels exhibited a compressive strength of 300 kPa, demonstrating excellent load-bearing performance. Compared to unloaded Hy hydrogels, loading with KGN did not significantly affect the compressive properties (Figure 3F and G). Compression tests using a mechanical testing machine revealed the unloading behavior of the hydrogel, indicating that Hy@KGN possesses excellent fatigue resistance (Figure 3H). Tensile tests revealed that Hy@KGN hydrogels had a tensile strength of 1.5 MPa and 150% elongation at break, indicating superior mechanical properties, with no significant changes compared to unloaded Hy hydrogels (Figures 3I, J and S5). Compared to the hydrogel without the loaded drug (Hy), the KGN-loaded hydrogel did not exhibit significant changes in mechanical properties.

The water absorption and swelling capacities of Hy and Hy@KGN were determined through hydration experiments. The results indicated that the Hy@KGN hydrogel exhibited an impressive SR of 400% within 24 h, demonstrating robust water absorption and swelling properties (Figure 3K). *In vitro* degradation experiments in simulated body fluid demonstrated that Hy@KGN hydrogels had approximately 20% mass loss over 8 weeks, suggesting a moderate degradation rate suitable for long-term tissue repair. Drug loading did not significantly alter the degradation behavior (Figure 3L). Adhesion strength tests indicated that Hy@KGN hydrogels achieved an adhesion strength of 0.8 MPa in cartilage repair regions, with comparable performance to unloaded Hy hydrogels. White-light images confirmed the tight bonding between Hy@KGN hydrogels and rat cartilage tissue (Figure 3M). Compared to the Hy hydrogel, the drug-loaded Hy@KGN hydrogel did not exhibit significant changes in stability or adhesiveness. Moreover, release experiments of KGN in a simulated body fluid environment demonstrated that Hy@KGN released 80% of KGN within the first 2 weeks, followed by a slow-release phase, thus continuously delivering KGN to facilitate cartilage repair (Figure 3N).

3.3. Hy@KGN significantly enhances chondrogenic differentiation of BMSCs and mitigates inflammation

Bone marrow stromal cells (BMSCs) were divided into the following four treatment groups: PBS, Hy hydrogel, KGN, and Hy@KGN hydrogel. Cell viability was assessed via the CCK-8 assay, demonstrating over 90% viability across all groups, suggesting minimal cytotoxicity of the materials (Figure 4A). This finding was further supported by live/lead fluorescence staining, where live cells were stained green and dead cells were stained red, with no significant differences observed among the groups (Figure 4B).

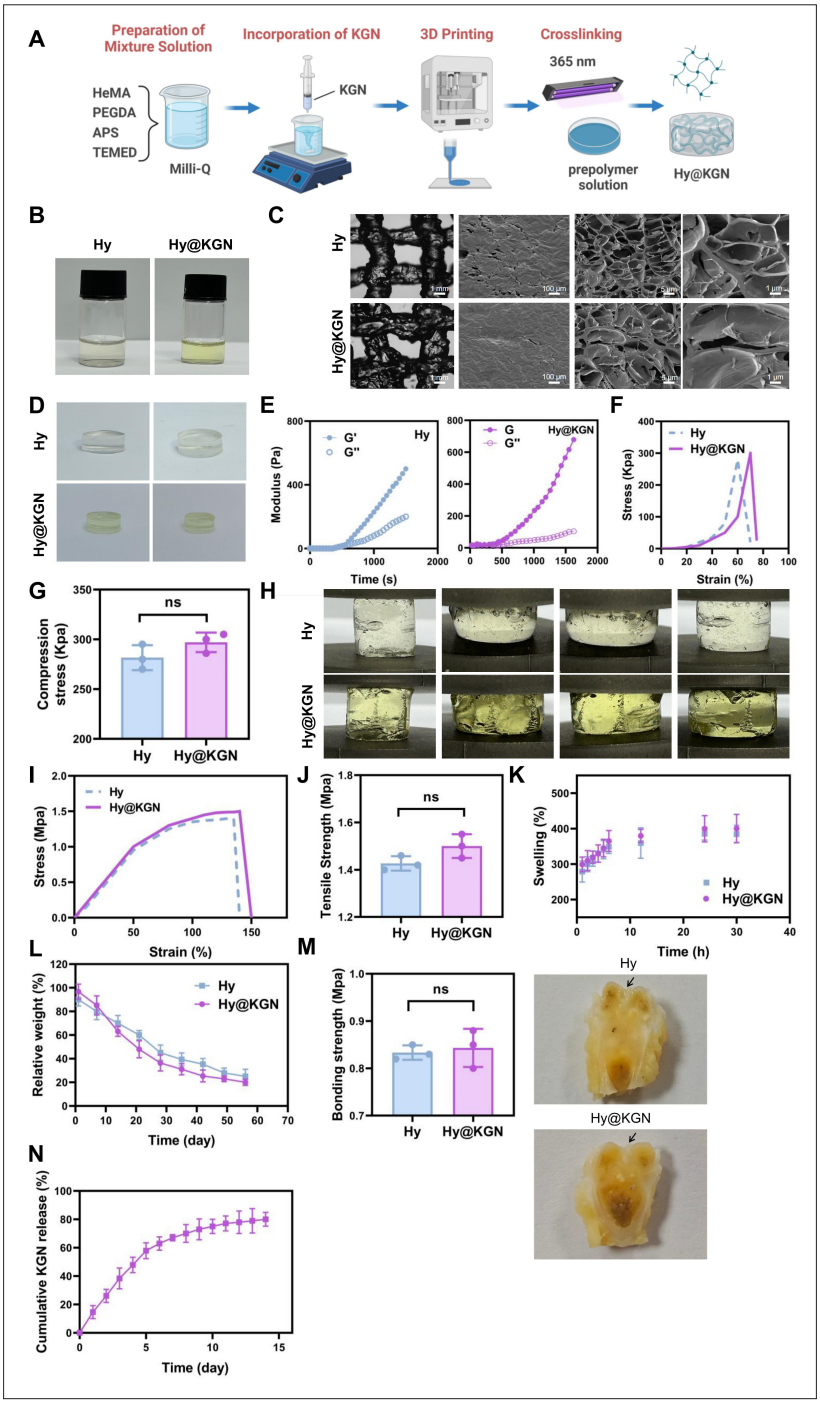

Figure 3. Preparation and characterization of Hy@KGN. (A) Schematic of the preparation process for Hy@KGN. (B) Bright-field images of Hy and Hy@KGN hydrogels. (C) Microstructure of the 3D-printed hydrogel observed under SEM at different magnifications. (D) Bright-field images of disc-shaped Hy and Hy@KGN hydrogels. (E) Rheological measurements of *G*' and *G*" of the 3D-printed hydrogel. (F) Representative compressive stress–strain curves for Hy and Hy@KGN hydrogels. (G) Average compressive strength of Hy and Hy@KGN hydrogels. (H) Compression testing process for Hy and Hy@KGN hydrogels using a mechanical tester. (I) Representative tensile stress–strain curves for Hy and Hy@KGN hydrogels. (J) Average tensile strength of Hy and Hy@KGN hydrogels. (K) SR of Hy and Hy@KGN hydrogels determined through water absorption experiments. (L) *In vitro* degradation behavior of Hy and Hy@KGN hydrogels. (M) Adhesion strength of Hy and Hy@KGN hydrogels in the cartilage repair region, along with bright-field images displaying the bonding interface between Hy@KGN hydrogel and cartilage tissue. (N) KGN release profile of Hy@KGN hydrogel in a simulated body fluid environment; $n = 3$. Scale bars: 1 mm (C). Abbreviations: APS, ammonium persulfate; *G*′, storage modulus; *G*″, loss modulus; HeMA, 2-hydroxyethyl methacrylate; Hy, hydrogel without kartogenin; KGN, Kartogenin; Milli-Q, Ultrapure water; ns, not significant; PEGDA, poly(ethylene glycol) diacrylate; TEMED, N,N,N′,N′-tetramethylethylenediamine.

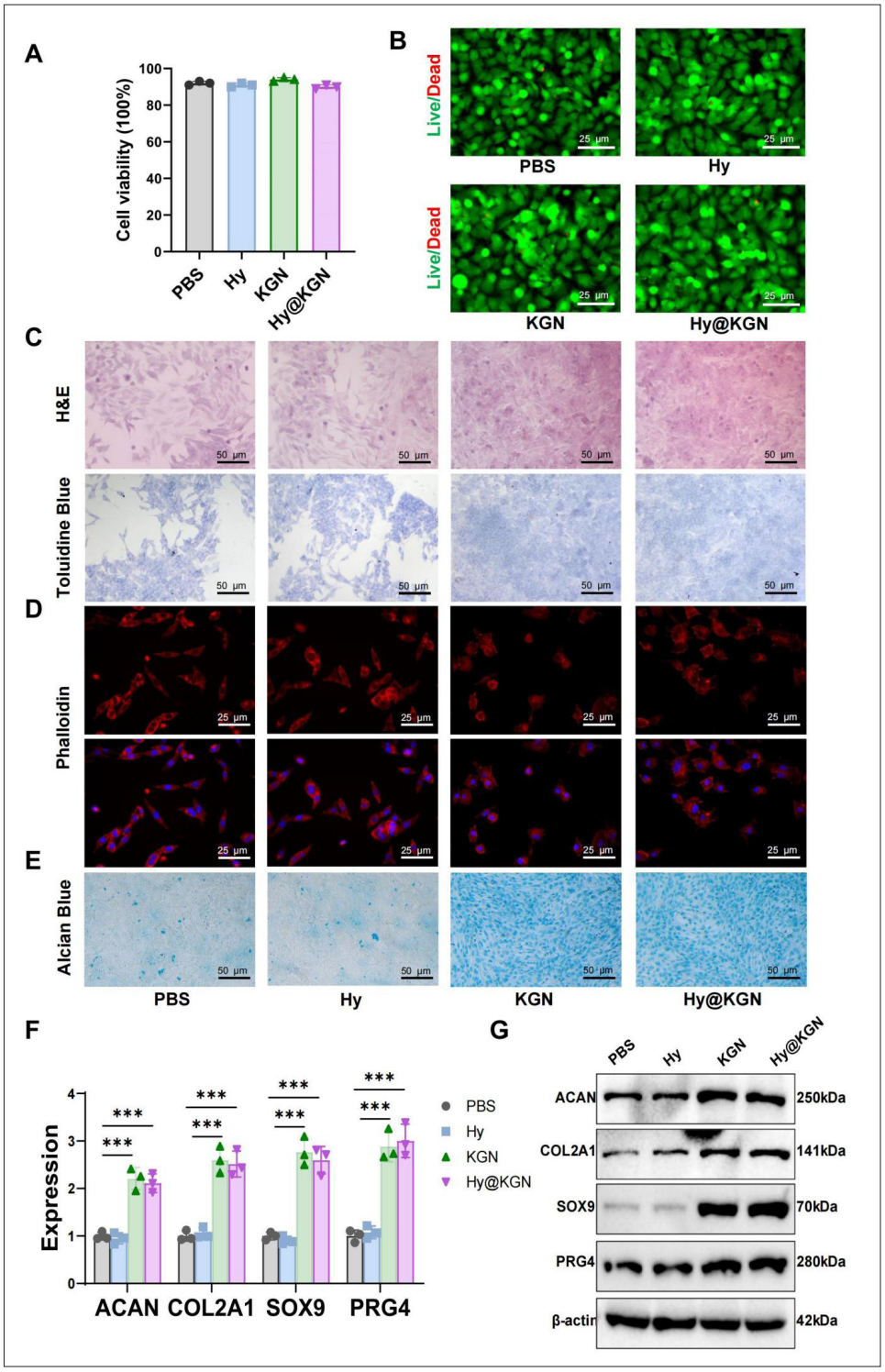

Figure 4. Effects of Hy@KGN hydrogel on chondrogenic differentiation of BMSCs. (A) CCK-8 assay evaluated the cytotoxicity of each treatment on BMSCs. (B) Live/dead fluorescence staining of BMSCs in each treatment group. (C) Toluidine blue and H&E staining of cartilage tissue appearance in BMSCs from different treatment groups. (D) Phalloidin staining to observe morphological changes of BMSCs in different treatment groups. (E) Alcian blue staining to assess chondrogenic differentiation of BMSCs. (F) RT-qPCR analysis of chondrogenesis-related genes: *Col2a1*, *Acan*, *Sox9*, and *Prg4*. (G) Western Blot analysis of chondrogenesis-related protein expression. ***$p < 0.001$, ****$p < 0.0001$. All cell experiments were performed in triplicate. Data were tested for normality using the Shapiro–Wilk test and analyzed using one-way ANOVA with Tukey's HSD post hoc test for group comparisons. Scale bars: 25 μm (A, B, and D), 50 μm (C and E). Abbreviations: BMSCs, bone marrow stromal cells.

To assess the hydrogel's chondrogenic potential, BMSCs were cultured in chondrogenic medium supplemented with 2 μL of hydrogel extract solution (prepared by incubating Hy@KGN hydrogels in culture medium). Using this optimized volume ensured sufficient matrix support while avoiding excessive cell aggregation, balancing bioactivity with nutrient availability. The hydrogel extract enables uniform cell distribution within the medium, prevents clustering, and is easy to handle and mix with the medium. The concentration and volume can be adjusted as needed, providing better control of experimental conditions, with fresh medium changes daily over 21 days. Alcian blue and H&E staining results indicated that the cell morphology in the KGN and Hy@KGN hydrogel groups resembled cartilage tissue, indicating significant differentiation of BMSCs into chondrocytes. In contrast, no notable differences were observed in the PBS and Hy hydrogel groups (Figure 4C). In another experiment, BMSCs were mixed with Hy@KGN hydrogel precursor solution and cultured at 37 °C for 7 days with daily supplementation of rMMP-3 (25 ng/mL). Phalloidin staining results demonstrated that by Day 7, the cell morphology in the KGN and Hy@KGN hydrogel groups transitioned from spindle-shaped to the polygonal shape characteristic of chondrocytes, while the PBS and Hy hydrogel groups displayed no significant morphological changes (Figure 4D).

Additionally, BMSCs were seeded on the surface of hydrogels and cultured with regular medium changes for 7 days. Alcian blue staining confirmed effective chondrogenic differentiation in the KGN and Hy@KGN groups, whereas no notable changes were detected in the PBS and Hy hydrogel groups (Figure 4E). To further validate the induction of chondrogenesis within hydrogels, RT-qPCR and Western blot analyses were conducted. The results revealed marked upregulation of chondrogenic markers, including COL2A1, ACAN, PRG4, and SOX9, in the KGN and Hy@KGN hydrogel groups, with no significant alterations observed in the PBS and Hy hydrogel groups (Figure 4F and G).

In this experiment, the hydrogels used were fabricated by 3D printing technology. The results demonstrate that the 3D-printed KGN-loaded hydrogel scaffolds provided an excellent microenvironment for BMSCs, significantly promoting their chondrogenic differentiation.

Moreover, cartilage injury is often accompanied by an inflammatory response, where inflammatory factors released by M1 macrophages, such as TGF-α and IL-1β, rapidly accumulate in the cartilage microenvironment. These cytokines engage receptors on chondrocytes, triggering the IκBα/NF-κB pathway and promoting NF-κB translocation to the nucleus, thereby initiating cartilage degradation and upregulating MMPs (Figure S6A, Supporting Information). To assess the anti-inflammatory potential of Hy@KGN, chondrocytes were stimulated with IL-1β (10 ng/mL). Immunofluorescence analysis demonstrated that IL-1β induced nuclear translocation of NF-κB (green fluorescence), whereas KGN and Hy@KGN treatments markedly suppressed this effect, indicated by reduced nuclear staining (blue nuclei). In contrast, PBS and Hy hydrogel groups exhibited no inhibition (Figure S6B, Supporting Information). Western blot analysis demonstrated that the KGN and Hy@KGN hydrogel groups reduced the expression of COX-2, MMP-3, and phosphorylated NF-κB (p65) in chondrocytes, while the PBS and Hy hydrogel groups displayed no significant changes (Figure S6C and D, Supporting Information).

3.4. Hy@KGN activates the Smad1/5/9 signaling pathway to promote chondrogenic differentiation of BMSCs

To explore the involvement of a Hy@KGN in promoting chondrogenic differentiation of BMSCs, we divided the BMSCs into four groups: a PBS group, a Smad1/5/9 pathway inhibitor group (treated with LDN-193189), a Hy@KGN hydrogel group, and a group combining the Hy@KGN and the inhibitor (Figure 5A). Western blot analysis was conducted to measure the expression of Smad1/5/9 pathway-related factors in each group. The results demonstrated a significant increase in Smad1/5/9 protein expression in the Hy@KGN hydrogel group, whereas a notable decrease in the expression of these pathway-related factors was observed in both the Hy@KGN + inhibitor group and the LDN-193189 group (Figure 5B).

Alcian blue and H&E staining demonstrated that the inhibitor LDN-193189 significantly reduced the differentiation capability of BMSCs into chondrocytes (Figure 5C and D). Phalloidin staining indicated no significant changes in the morphology of BMSCs treated with LDN-193189 (Figure 5E). When BMSCs were seeded on the hydrogel surface and treated with LDN-193189 in the presence of rMMP-3, Alcian blue staining revealed that the inhibitor significantly reduced the chondrogenic differentiation capability of BMSCs (Figure 5F). To further confirm the chondrogenic differentiation within the hydrogel, we assessed cartilage-related protein expression using RT-qPCR and Western blot, which indicated that LDN-193189 could reverse the upregulation of COL2A1, ACAN, PRG4, and SOX9 promoted by the Hy@KGN hydrogel (Figure 5G and H).

Furthermore, in the inflammatory response of chondrocytes induced by IL-1β (10 ng/mL), immunofluorescence staining demonstrated that LDN-193189 reversed suppression of NF-κB nuclear translocation

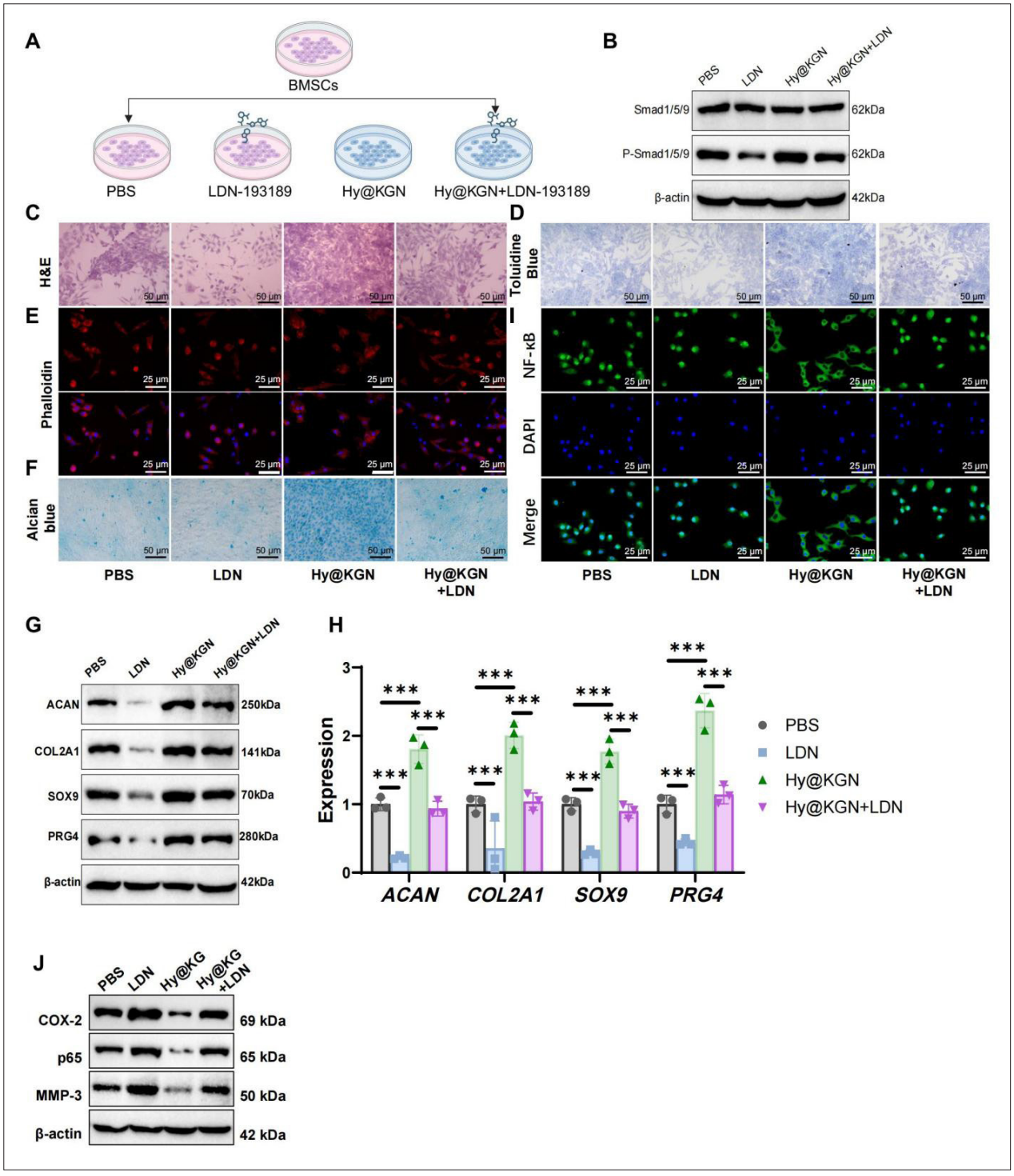

Figure 5. Effects of LDN-193189 inhibitor on chondrogenic differentiation of BMSCs. (A) Schematic of the experimental procedure. (B) Western blot analysis of Smad1/5/9 pathway-related factor expression. (C) H&E staining to assess the chondrogenic differentiation capacity of BMSCs. (D) Toluidine blue staining to assess the chondrogenic differentiation capacity of BMSCs. (E) Phalloidin staining to observe morphological changes in BMSCs. (F) Alcian blue staining to assess the chondrogenic differentiation capacity of BMSCs. (G) Western blot analysis of chondrogenesis-related proteins COL2A1, ACAN, PRG4, and SOX9. (H) RT-qPCR analysis of chondrogenesis-related genes *Col2a1*, *Acan*, *Prg4*, and *Sox9*. (I) Immunofluorescence staining to detect NF-κB nuclear translocation in chondrocytes. (J) Western blot analysis and quantification of COX-2, MMP-3, and phosphorylated NF-κB (p65) expression in chondrocytes. All cell experiments were performed in triplicate; ***$p < 0.001$. Scale bars: 25 μm (E and I); 50 μm (C, D, and F). Abbreviation: BMSCs, bone marrow stromal cells.

observed in the Hy@KGN hydrogel group (Figure 5I). Consistently, Western blot analysis revealed a marked upregulation of COX-2, MMP-3, and phosphorylated NF-κB (p65) following LDN-193189 treatment (Figure 5J). This part of the experiment was based on 3D-printed hydrogel scaffolds. Using a Smad1/5/9 pathway inhibitor, we further validated that the 3D-printed KGN-loaded hydrogel promotes BMSC chondrogenic differentiation by activating the Smad1/5/9 signaling pathway.

3.5. Biocompatibility of Hy@KGN

To verify the *in vivo* biosafety of Hy@KGN hydrogel, we implanted it subcutaneously in healthy rats and monitored their weight and behavior periodically, as illustrated in Figure 6A. Throughout the experiment, all rats demonstrated consistent weight gain without any observed abnormal behaviors or significant weight loss, indicating that the hydrogel implantation had no adverse effects on the physiological activities of the rats (Figure 6B).

Weekly blood samples were collected for complete blood count and biochemical assessments. All hematological parameters remained within physiological limits, indicating no systemic abnormalities (Table 2). Serum biochemical indices, including ALT, AST, BUN, and Cr, displayed no significant deviations from normal reference values throughout the observation period, suggesting that the Hy@KGN hydrogel implantation did not exert any significant toxicity on liver or kidney functions (Figure 6C). Post-experiment, the major organs (liver, kidney, spleen, heart, and lungs) were subjected to H&E staining, which revealed no significant pathological changes or inflammation, with normal tissue architecture and no signs of cellular infiltration or necrosis (Figure 6D).

Furthermore, TUNEL staining indicated low levels of apoptosis at the hydrogel implantation sites, with no significant differences compared to normal tissue (Figure 6E and F). Immunohistochemical (IHC) analysis revealed that the number of Bcl-2–positive cells, characterized by brown-stained cytoplasm, did not differ significantly between the Hy@KGN and control groups (Figure 6G). ELISA results for serum inflammatory markers, such as IL-6 (Figure 6H), TNF-α (Figure 6I), and IL-1β (Figure 6J), exhibited no significant increase, indicating that the implant did not trigger a systemic inflammatory response. These results demonstrate that the Hy@KGN hydrogel possesses excellent biosafety and is suitable for *in vivo* applications.

3.6. Hy@KGN significantly enhances cartilage repair in rats via the Smad 1/5/9 pathway

To assess the potential of this hydrogel for *in vivo* cartilage repair potential of the hydrogel, a full-thickness cartilage defect model was established in Sprague-Dawley rats and divided into the following five groups: PBS control, Hy hydrogel, KGN, Hy@KGN hydrogel, and LDN+Hy@KGN. Each material was implanted into the defect area, with evaluations conducted 6 and 12 weeks post-surgery (the experimental process depicted in Figure 7A). Observations and histological analyses at 6 weeks postoperation (Figure S7A and B, Supporting Information) revealed tissue

Table 2. Complete blood count

Variable	Control ($n = 9$)	Hy ($n = 10$)	KGN@Hy ($n = 10$)
WBC (10^6/4)	3.87 ± 0.72	4.25 ± 1.19	4.01 ± 0.55
RBC (10^6/4)	7.31 ± 0.20	7.38 ± 0.90	7.48 ± 0.32
Hemoglobin (g/dL)	141.59 ± 10.30	141.85 ± 7.85	139.93 ± 8.41
Hematocrit (%)	42.55 ± 4.16	44.58 ± 5.57	43.15 ± 5.03
MCV (fL)	61.08 ± 6.85	60.72 ± 5.81	60.76 ± 2.01
MCH (pg)	19.59 ± 0.22	19.83 ± 0.33	20.35 ± 0.57
MCHC (pg)	324.45 ± 9.32	330.23 ± 11.25	324.55 ± 10.46
Platelet (10^3/4)	1.03 ± 0.19	0.98 ± 0.12	1.04 ± 0.67
RDW-SD (fL)	31.66 ± 1.44	31.72 ± 5.23	31.35 ± 5.11
RDW-CV (%)	13.89 ± 0.98	14.76 ± 2.79	13.20 ± 0.62
Reticulocytes (%)	1.92 ± 0.67	2.15 ± 0.34	1.87 ± 0.43
NRBC (/100 WBC)	0.22 ± 0.15	0.18 ± 0.13	0.83 ± 0.09

Note: Each value represents the mean ± standard deviation. The *p*-values were calculated compared to the control group (*$p < 0.05$). Abbreviations: MCH, mean corpuscular hemoglobin; MCHC, mean corpuscular hemoglobin concentration; MCV, mean corpuscular volume; NRBC, nucleated red blood cell; RBC, red blood cell; RDW-SD, red cell distribution width–standard deviation; RDW-CV, red cell distribution width–coefficient of variation; WBC, white blood cell.

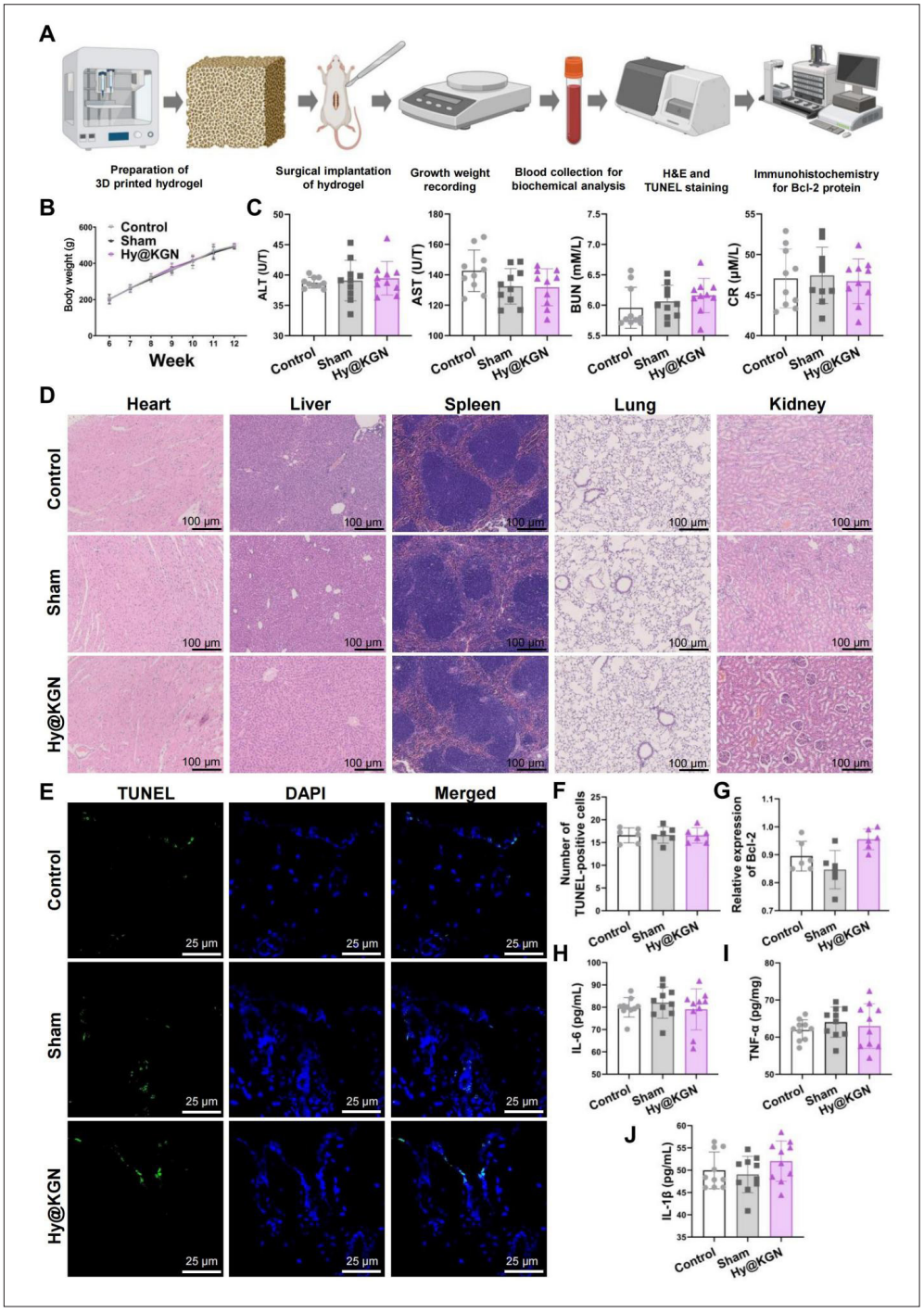

Figure 6. *In vivo* biosafety evaluation of Hy@KGN hydrogel. (A) Technical flowchart illustrating the biosafety assessment procedure. (B) Monitoring of body weight changes in each group of rats (n = 10). (C) Blood biochemical analysis of liver function (ALT, AST) and kidney function (BUN, Cr) levels in rats (n = 10). (D) H&E staining of heart, liver, spleen, lung, and kidney tissues to observe tissue structure and pathology in each group (n = 10). (E) TUNEL staining to detect apoptotic cells in tissues on Day 7 (n = 10). (F) Quantification of TUNEL-positive cells (n = 6). (G) Immunohistochemical staining for Bcl-2 expression in tissues on Day 7 (n = 6). (H–J) ELISA analysis of serum levels of inflammatory factors: IL-6 (H), TNF-α (I), and iNOS (J) (n = 10). All cell experiments were performed in triplicate. Data were tested for normality using the Shapiro–Wilk test and analyzed using one-way ANOVA with Tukey's HSD post hoc test for group comparisons. Scale bars: 100 μm (D); 25 μm (E). Abbreviations: ALT, alanine aminotransferase; AST, aspartate aminotransferase; Bcl-2, B-cell lymphoma-2; BUN, blood urea nitrogen; CR, creatinine; DAPI, 4′,6-diamidino-2-phenylindole; H&E, Hematoxylin and eosin; Hy@KGN, Kartogenin-loaded hydrogel; IL-6, Interleukin-6; IL-1β, Interleukin-1 beta; TNF, tumor necrosis factor; TUNEL, terminal deoxynucleotidyl transferase-mediated dUTP nick-end labeling.;;;; …

regeneration at the defect sites in all groups, although the new cartilage tissue had not yet fully covered the injured areas. The PBS control group displayed the most distinct boundary between the regenerated area and the original cartilage, whereas the Hy@KGN group displayed more seamless integration, likely due to enhanced BMSC survival and chondrogenic differentiation supported by the hydrogel. Consistent with macroscopic observations, the H&E staining revealed disorganized fibrous tissue architecture and lower subchondral bone reconstruction in the PBS and Hy groups. In contrast, the KGN and Hy@KGN groups exhibited more organized repair tissues, indicating accelerated bone reconstruction, though boundaries were still present. SO/FG staining demonstrated the onset of cartilage differentiation, with minimal differentiation in the PBS and LDN+Hy@KGN groups, while the other groups exhibited partial cartilage differentiation, indicating active matrix secretion at this stage, with the Smad 1/5/9 pathway playing a crucial role in the process.

At 12 weeks post-surgery, the defect area displayed a significant increase in the filling rate of repair tissue, with nearly no residual hydrogel visible (Figure S7C, Supporting Information). In the PBS and LDN+Hy@KGN groups, the repair tissue remained recessed relative to the surrounding cartilage and exhibited surface irregularities. In contrast, the KGN and Hy@KGN groups displayed repair tissue that was level with native cartilage and exhibited a smooth, cartilage-like morphology. The Hy group primarily formed fibrous tissue, while the Hy@KGN group featured a more seamless integration between repair and native cartilage compared to the KGN group (Figure S7C, Supporting Information). Repair tissue in the PBS and Hy groups was mainly fibrous, with limited response to SO/FG staining (Figure S7D, Supporting Information). Compared to the PBS and LDN+Hy@KGN groups, the Hy group exhibited improved subchondral bone reconstruction with fewer fissures. The Hy@KGN and KGN groups displayed more substantial cartilage-like new tissue, with the Hy@KGN group presenting more uniform and mature repair cartilage. Notably, SO/FG staining displayed more intense red staining in the Hy@KGN group, indicating a faster cartilage repair rate and higher proteoglycan content than the KGN group. Combined with *in vitro* findings, the 12-week repair outcome likely relates to enhanced BMSC and chondrocyte activity and accelerated matrix synthesis within the defect area, thereby promoting cartilage repair.

Subchondral bone reconstruction was evaluated using micro-CT. At Week 6, all groups exhibited varying degrees of bone defects, with the Hy@KGN and KGN groups displaying the most limited damage (Figure 7B). By Week 12, the subchondral bone in the Hy@KGN group was almost fully reconstructed (Figure 7C). Quantitative evaluation revealed significantly higher BV/TV and BMD values, and reduced BDV/TV and Tb.Sp in the Hy, KGN, and Hy@KGN groups compared to PBS, with the Hy@KGN group exhibiting the most pronounced improvements. However, these effects in the Hy@KGN group were reversed by LDN (Figure 7D–F). The Smad1/5/9 signaling pathway plays a critical role in inducing bone formation; Western blot analysis demonstrated that at both Weeks 6 and 12 post-surgery, the Hy@KGN and KGN groups significantly promoted Smad1/5/9 protein phosphorylation, while phosphorylation levels in the inhibitor group remained low (Figure 7G and H). These findings, supported by H&E, SO/FG staining, and micro-CT data, indicate that the inhibitor group had poorer cartilage repair outcomes, demonstrating that KGN's ability to enhance subchondral bone reconstruction improves over time, with the Hy@KGN hydrogel outperforming KGN alone in this regard.

Additionally, Alcian blue staining at 6 weeks post-surgery indicated significantly higher levels of blue-stained cartilage matrix (hyaluronic acid and acidic glycosaminoglycans) in the KGN and Hy@KGN groups compared to the PBS and Hy groups, with the Hy@KGN group exhibiting the most extensive positive staining. This effect of Hy@KGN was reversed by LDN (Figure 8A and C). Sirius red staining confirmed the presence of collagen types I and II, a finding further supported by IHC results (Figure 8A and D–F). At 12 weeks post-surgery, Alcian blue staining revealed uniform cartilage matrix distribution in all groups except the PBS and LDN+Hy@KGN groups (Figure 8B and C). However, at Week 12, the cartilage matrix in both the KGN and Hy@KGN groups appeared thinner than at Week 6, likely due to ongoing subchondral bone remodeling that led to partial replacement by fibrous or cartilage-like tissue. Notably, the Hy@KGN group exhibited blue staining patterns closely matching those of adjacent native cartilage, indicating more advanced regeneration than the KGN group. IHC and quantitative analysis further confirmed that the Hy@KGN group achieved the most effective cartilage repair, with the highest collagen I and collagen II expression levels in the regenerated cartilage tissue (Figure 8B and D–F). According to the ICRS macroscopic scoring system, repair scores in the Hy, KGN, and Hy@KGN hydrogel groups at Week 6 were higher than in the PBS group, with LDN reversing the repair effects of Hy@KGN hydrogel (Figure 8G). Masson's trichrome staining indicated significantly greater deposition of newly formed collagen at the cartilage defect sites in the Hy@KGN group (Figure 8H and I).

These results demonstrate that the Hy@KGN hydrogel performs well in promoting cartilage regeneration,

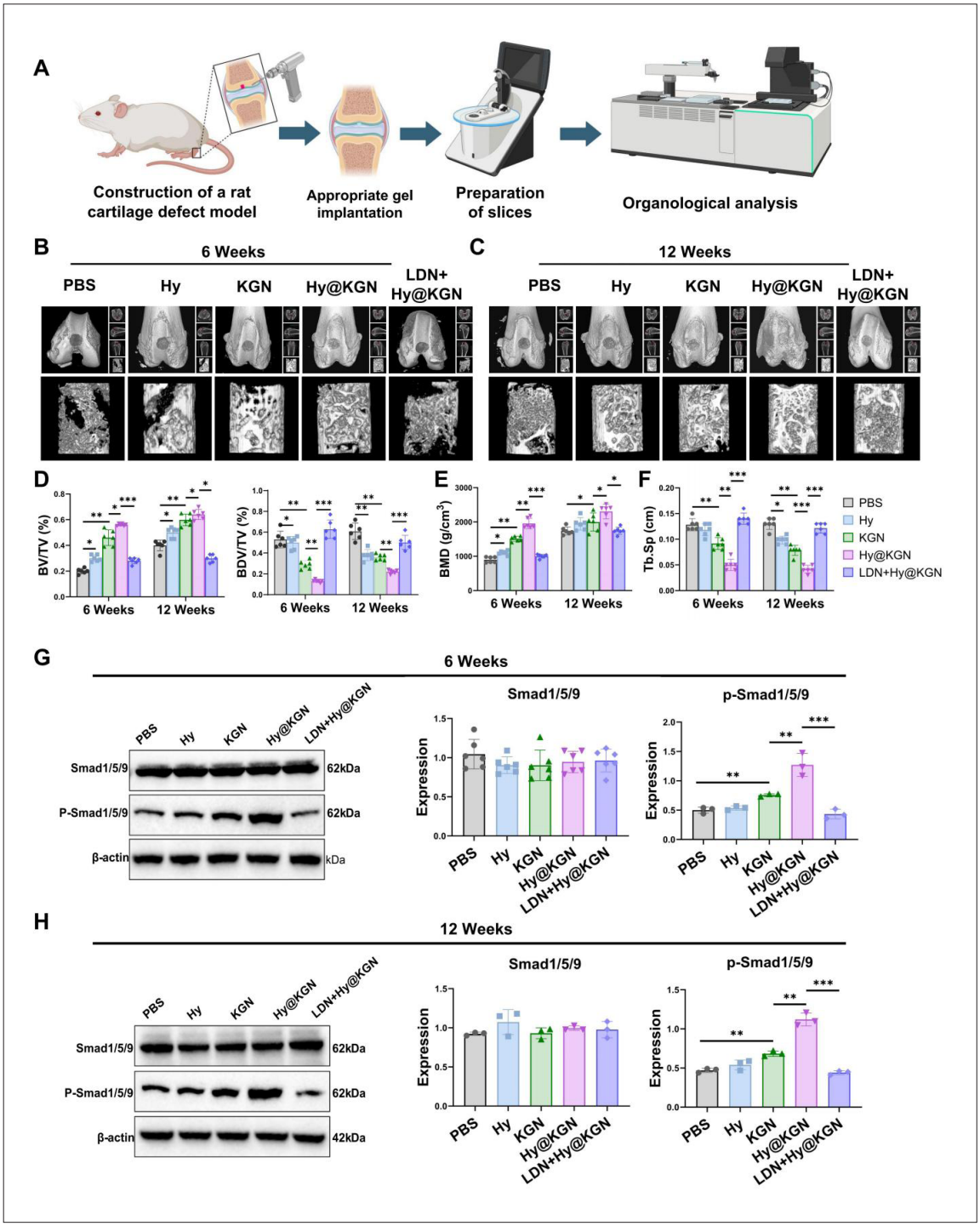

Figure 7. Evaluation of *in vivo* cartilage regeneration potential of Hy@KGN hydrogel. (A) Schematic of the surgical procedure. (B) Micro-CT imaging presents new cartilage formation at 6 weeks post-surgery. (C) Micro-CT imaging presents new cartilage formation at 12 weeks post-surgery; the red dashed line indicates the defect area. (D–F) Quantification of BV/TV and BDV/TV (D), BMD (E), and Tb.Sp (F). (G) Western blot analysis of phosphorylated and non-phosphorylated Smad1/5/9 protein levels at 6 weeks post-surgery in each group. (H) Western blot analysis of phosphorylated and non-phosphorylated Smad1/5/9 protein levels at 12 weeks post-surgery in each group (n = 6 rats per group); * $p < 0.05$, ** $p < 0.01$, *** $p < 0.001$. All cell experiments were performed in triplicate. Data were tested for normality using the Shapiro–Wilk test and analyzed using one-way ANOVA with Tukey's HSD post hoc test for group comparisons. Scale bars: 2 mm (B and C). Abbreviations: β-actin, beta actin; BV/TV, bone volume/tissue volume; BMD, bone mineral density; Hy, hydrogel; Hy@KGN, kartogenin-loaded hydrogel; KGN, kartogenin; LDN, LDN-193189 (BMP pathway inhibitor); PBS, phosphate-buffered saline; P-Smad1/5/9, phosphorylated Smad1/5/9; Smad1/5/9, mothers against decapentaplegic homolog 1/5/9; Tb.Sp, trabecular separation.

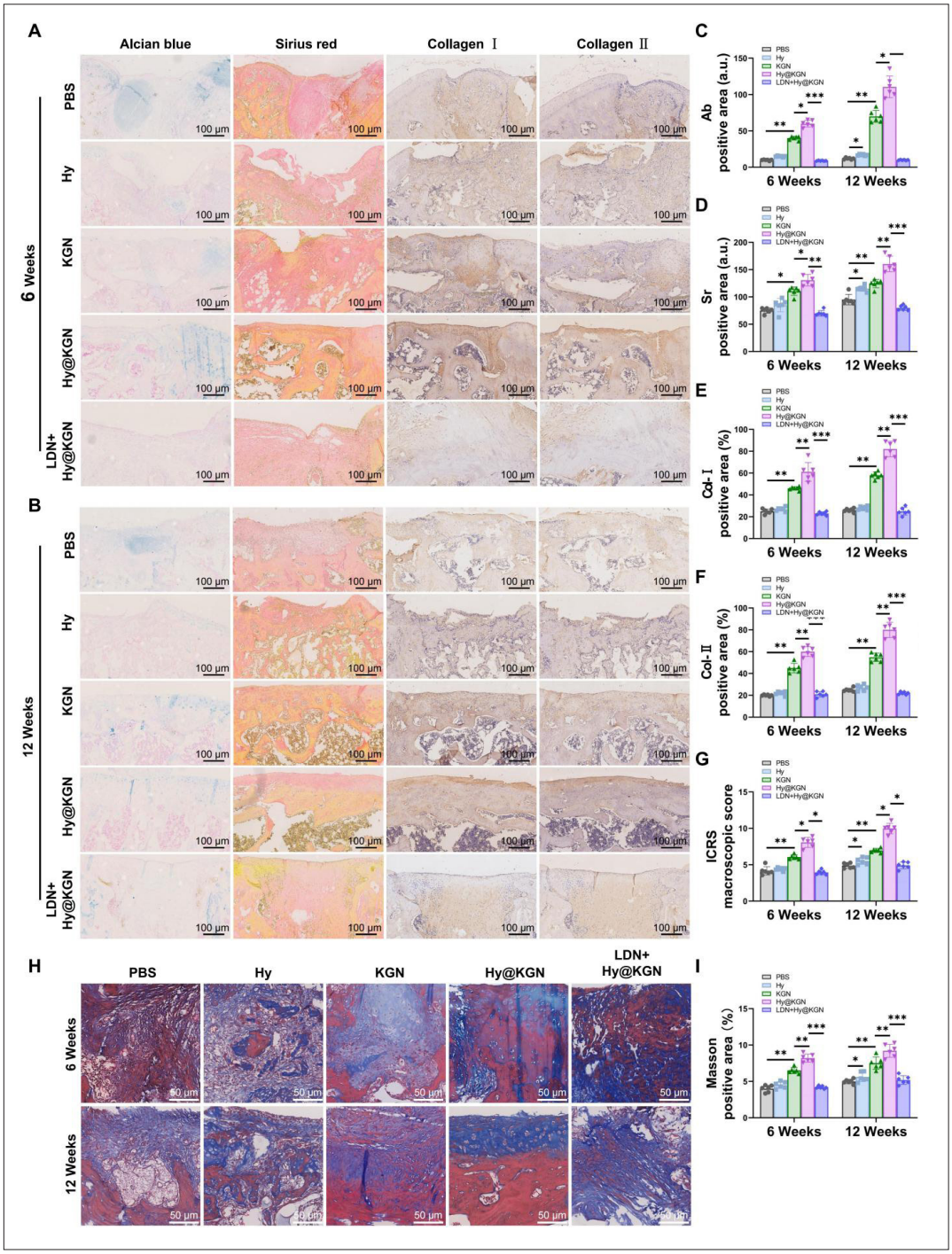

Figure 8. Assessment of cartilage regeneration by Hy@KGN hydrogel in full-thickness cartilage defect model in Sprague-Dawley rats. (A) Alcian blue staining for cartilage proteoglycans, Sirius red staining for collagen fibers, and immunohistochemical staining for collagen types I and II at 6 weeks post-surgery. (B) Alcian blue staining for cartilage proteoglycans, Sirius red staining for collagen fibers, and immunohistochemical staining for collagen types I and II at 12 weeks post-surgery. (C) Quantitative analysis of Alcian blue staining. (D) Quantitative analysis of Sirius red staining. (E) Quantitative analysis of collagen I immunohistochemical staining. (F) Quantitative analysis of collagen II immunohistochemical staining. (G) ICRS macroscopic scoring system for evaluating repair cartilage. (H) Masson's trichrome staining of collagen deposition at 6 and 12 weeks post-surgery across groups. (I) Quantification of collagen deposition across groups. $n = 6$ rats per group; $^{*}p < 0.05$, $^{**}p < 0.01$, $^{***}p < 0.001$. Scale bars: 100 μm (A and B); 50 μm (H). Abbreviations: Alcian blue, Alcian blue staining; Col I, collagen type I; Col II, collagen type II; Hy, hydrogel; Hy@KGN, kartogenin-loaded hydrogel; ICRS, International Cartilage Repair Society; KGN, kartogenin; LDN, LDN-193189 (BMP pathway inhibitor); Odr-1α, osteogenic differentiation-related protein 1 alpha; PBS, phosphate-buffered saline; Sirius red, Sirius red staining.

highlighting its potential as a clinical scaffold material for cartilage repair.

4. Discussion

Cartilage injuries are challenging to treat due to the tissue's limited self-repair capacity. Traditional treatments, such as drug therapy and surgical implants, can alleviate symptoms to some extent but often fall short of achieving ideal repair outcomes.[23] As a result, patients frequently rely on non-curative approaches, including pain management and functional support, which can significantly impact their quality of life over the long term.[24] Recently, 3D printing technology has demonstrated immense potential in biomedical engineering, primarily due to its ability to precisely control material structure and function.[1,3] As a novel delivery vehicle, 3D-printed hydrogel efficiently transports bioactive molecules and provides an environment that mimics the natural ECM, essential for promoting chondrocyte growth and new cartilage formation.[25] This technology addresses the limitations of traditional cartilage repair methods and offers patients a more effective and durable treatment option.[26]

The 3D-printed hydrogel used in this study combines biocompatibility with superior mechanical properties, distinguishing it from conventional cartilage repair materials.[27] Previous research has primarily focused on natural materials, such as collagen and hyaluronic acid, which provide some structural support but often lack the necessary mechanical strength and flexibility for complex cartilage defect applications.[28] In contrast, the synthetic hydrogel in this study, fabricated with precise 3D printing technology, can replicate more intricate biological structures at the microscopic level, a feat challenging to achieve with traditional materials. Additionally, incorporating the small molecule compound KGN through 3D printing introduces an innovative approach by directly modulating stem cell behavior with chemical agents, a relatively rare strategy in prior studies. This approach enhances the efficiency and controllability of stem cell therapy and opens new pathways for future research in regenerative medicine.

In this study, we developed a precise and sustained delivery strategy for KGN by combining 3D bioprinting technology with a HEMA- and PEGDA-based hydrogel formulation, which significantly improved the efficiency of BMSC chondrogenic differentiation. Compared with previously reported dynamic hydrogels crosslinked through host–guest interactions,[29] our delivery system demonstrates higher efficiency and controllability. In addition, compared with the results of BMSC-laden 3D-bioprinted scaffolds reported by Wang *et al.*,[9] our hydrogel demonstrated superior comprehensive performance and more significant cartilage repair outcomes. Moreover, while another study[30] utilized dual-cell living hydrogels, our delivery strategy is more precise and better simulates the natural cartilage microenvironment. Compared with microfluidic-generated hydrogel microspheres,[31] our approach is more suitable for large-scale production and clinical application. Furthermore, compared with studies directly investigating KGN's effect on the osteogenic differentiation of BMMSCs,[32] this study integrates 3D bioprinting technology and systematically elucidates the underlying mechanisms of KGN's action, verifying its efficacy *in vivo* with significantly improved repair effects. Unlike prior studies, we combined RNA-seq, WGCNA, and PPI network analysis to comprehensively reveal the core regulatory role of the Smad1/5/9 signaling axis at both the transcriptomic and protein levels.

Previous studies have demonstrated that the TGF-β pathway promotes chondrocyte proliferation and ECM synthesis by activating the Smad2/3 pathway through its receptors.[33] The Wnt pathway facilitates chondrocyte differentiation through β-catenin accumulation and nuclear translocation.[34] However, in this study, we focused primarily on the Smad1/5/9 pathway for several reasons. Firstly, our RNA-seq differential expression analysis, WGCNA module screening, and PPI network construction consistently indicated that Smad1, Smad5, and Smad9 were significantly upregulated following KGN treatment and occupied core positions within the regulatory networks. This multilevel evidence indicates the critical role of the Smad1/5/9 axis in KGN-induced BMSC chondrogenic differentiation. Secondly, existing studies have demonstrated that activation of the Smad1/5/9 pathway significantly upregulates genes essential for cartilage formation, such as *SOX9* and *COL2A1*, which are vital for chondrocyte maturation and matrix synthesis. Although the Smad2/3 pathway can also contribute to cartilage formation, its effect appears to be relatively modest. Additionally, activation of the Smad1/5/9 pathway can influence the Wnt signaling pathway by regulating downstream gene expression, thereby further promoting chondrocyte differentiation.[33] For these reasons, our study emphasizes the Smad1/5/9 pathway.

The Smad1/5/9 signaling pathway is a crucial intracellular signaling route primarily regulated by activating bone morphogenetic proteins (BMPs). Activation of this pathway begins with BMPs binding to their cell surface receptors, initiating receptor phosphorylation, which subsequently activates downstream Smad1, Smad5, and Smad9 proteins.[35] These phosphorylated Smads subsequently form a complex with the common mediator Smad4, which translocates into the nucleus to regulate the

transcription of downstream target genes.[36] This process is central to various biological functions, particularly in cell differentiation (e.g., BMSC differentiation into osteocytes or chondrocytes), tissue development, and repair, making it a key mechanism in bone and cartilage formation.[37,38]

Our study results demonstrate that KGN significantly activates the Smad1/5/9 signaling pathway, aligning closely with previous findings and further validating the pathway's pivotal role in regulating the chondrogenic differentiation of BMSCs. Activation of this pathway promotes the upregulation of chondrogenic differentiation-related genes and provides critical insights into the molecular mechanisms underlying BMSC differentiation. Unlike other studies using growth factors such as TGF-β to induce differentiation, KGN offers a simpler, more flexible, and efficient approach to cellular differentiation. As a small-molecule compound, KGN can readily penetrate the cell membrane and precisely activate target signaling pathways, thereby avoiding the immune reactions and high costs associated with growth factors. The advantages of this small-molecule induction strategy include lower production and storage costs and increased control and specificity, making it well-suited for large-scale clinical applications and presenting a promising avenue for widespread adoption.

The 3D-printed hydrogel developed in this study demonstrates excellent biocompatibility and mechanical properties. Compared to traditional cartilage repair materials, this novel hydrogel better replicates the physical characteristics of natural cartilage, such as elasticity and resilience, thereby creating an ideal microenvironment for cell adhesion, proliferation, and differentiation. Traditional materials often struggle to balance mechanical strength and elasticity; however, this hydrogel achieves that balance through optimized material composition and 3D printing technology, effectively supporting functional cell growth. Furthermore, water absorption and *in vitro* degradation assessments confirm its suitability for *in vivo* applications, showcasing significant advantages in maintaining structural integrity and enabling controlled degradation post-implantation. These improvements are critical for sustaining long-term cartilage repair effects, reducing the need for secondary surgeries, and enhancing cell-material interactions, providing a solid foundation for future clinical applications.

Through comprehensive *in vitro* and *in vivo* experiments, this study thoroughly evaluated the functionality of the 3D-printed hydrogel. *In vitro* results revealed that KGN significantly promotes chondrogenic differentiation of BMSCs, while *in vivo* experiments confirm the hydrogel's effectiveness in actual cartilage repair. This consistency highlights the reliability of the 3D-printed hydrogel as a cartilage repair material and points to subtle differences that may arise under varying experimental conditions, guiding future research adjustments.

Despite the significant *in vitro* and *in vivo* results demonstrating the potential of the 3D-bioprinted KGN-loaded hydrogel to promote BMSC chondrogenic differentiation and cartilage repair, there are still some limitations. Although we detected a significant increase in phospho-Smad1/5/9 expression by Western blot, we did not perform double IHC staining for phospho-Smad1/5/9 and Smad4 to directly verify the nuclear translocation of the Smad1/5/9–Smad4 complex. This process is crucial for confirming the activation mechanism of the Smad1/5/9 pathway, and future studies should consider double IHC staining to directly visualize this nuclear translocation. Moreover, although we characterized the hydrogel's rheological properties and observed its uniform microporous structure by SEM, we did not experimentally verify how the macroscopic architecture influences its rheological behavior. This verification is crucial for elucidating the relationship between macrostructure and rheological performance. Future studies should include more systematic experiments to address this gap and further optimize the material's properties for biomedical applications. Additionally, the observation of BMSC morphological changes has certain limitations. The cell images presented in Figure 4D were obtained by mixing BMSCs with the Hy@KGN hydrogel precursor solution and then performing phalloidin staining. Although this approach features morphological changes after co-culture with the precursor solution, it does not fully reflect the actual behavior of cells within the 3D hydrogel environment. 3D culture data could more intuitively demonstrate cell distribution, migration, and morphological dynamics within the hydrogel, providing a more comprehensive understanding of cell–material interactions. In future work, we will introduce advanced 3D cell culture techniques and multidimensional imaging methods, such as bioprinting, confocal microscopy, and cell labeling technologies, to directly observe BMSC distribution, migration, and morphological changes within the hydrogel. These improvements will enable a more comprehensive evaluation of Hy@KGN's effects on cell differentiation, providing more reliable evidence for cartilage repair material development. Finally, we did not assess the expression changes of BMP ligands (e.g., BMP2, BMP4, BMP6) directly; therefore, it remains unclear whether Hy@KGN activates the Smad1/5/9 pathway by upregulating these ligands. Although our RNA-seq results indicated upregulation of *Acan*, *Bmp2*, and *Bmp6* (Figure 1D), these findings only indirectly

suggest that BMP ligands may be involved. There is also a lack of direct evidence regarding the activation status of BMP receptors (BMPR1A, BMPR1B, BMPR2). Thus, we could not confirm whether Hy@KGN activates the Smad1/5/9 pathway through receptor phosphorylation or conformational changes. Moreover, since crosstalk exists between the Smad1/5/9 pathway and other pathways, such as Wnt and TGF-β, the absence of upstream receptor activation analysis limits our understanding of potential pathway cross-regulation. Future research should focus on examining whether Hy@KGN regulates BMP ligand expression and BMP receptor activation to clarify whether the pathway is initiated through ligand upregulation or receptor activation. Additionally, exploring crosstalk with other pathways (e.g., Wnt and TGF-β) will help further elucidate the mechanism by which Hy@KGN promotes chondrogenesis. Despite the promising outcomes, challenges remain for the long-term clinical application of 3D-printed hydrogels, including potential issues related to material stability and chronic inflammation. Future research should evaluate the hydrogel's long-term performance *in vivo*, particularly in animal models that mimic more complex clinical scenarios.

This study successfully developed a novel hydrogel by integrating 3D printing technology with the small molecule KGN, demonstrating outstanding efficacy in promoting BMSC chondrogenic differentiation and cartilage repair. These results enhance our understanding of the Smad1/5/9 pathway in chondrogenic differentiation and offer a new material option for treating related clinical conditions. Nonetheless, certain limitations remain, such as the need to further validate long-term biocompatibility and mechanical performance in clinically relevant models. Future studies will aim to optimize the hydrogel's chemical and physical properties and test in models that more closely replicate human physiological conditions.

5. Conclusion

This study successfully synthesized and characterized a Hy@KGN hydrogel, demonstrating its effectiveness in promoting the chondrogenic differentiation of BMSCs. Through a series of *in vitro* experiments, we found that the Hy@KGN hydrogel significantly enhances BMSC proliferation and chondrogenic differentiation while upregulating chondrogenic differentiation-related genes and proteins via activating the Smad1/5/9 signaling pathway.

This research elucidates the molecular mechanism by which the Hy@KGN promotes BMSC chondrogenic differentiation through Smad1/5/9 pathway activation. This finding offers new insights for developing cartilage repair materials. The composite material exhibits excellent biocompatibility and mechanical properties and significantly promotes cartilage regeneration, suggesting strong potential for clinical application. The material holds promise for treating cartilage injuries and degenerative joint diseases, offering patients an effective repair approach. Although substantial results were achieved in *in vitro* experiments, further studies are required to confirm its effectiveness *in vivo*. Additionally, the long-term biosafety and degradation behavior of the Hy@KGN warrants further investigation. The next steps in this research will involve animal model experiments to verify the composite material's efficacy *in vivo* for cartilage repair and to assess its potential side effects and safety profile. With continued technological advancements and deeper research, the Hy@KGN hydrogel is expected to become a valuable tool in cartilage repair, offering new solutions for treating cartilage injuries.

Acknowledgments

None.

Funding

This study was supported by the National Natural Science Foundation of China (81960403, 82060405, and 82360436); Lanzhou Science and Technology Plan Program (2021-RC-102); Natural Science Foundation of Gansu Province (22JR5RA943, 22JR5RA956, and 23JRRA1500); Cuiying Scientific and Technological Innovation Program of Lanzhou University Second Hospital (CY2021-MS-A07).

Conflict of interest

The authors declare no conflict of interest.

Author contributions

Conceptualization: Yayi Xia
Formal analysis: Rongjin Cheng, Fei Yang
Funding: Yayi Xia
Investigation: Chenhui Yang, Changshun Chen, Hefang Xiao, Bin Geng
Methodology: Chenhui Yang, Changshun Chen
Supervision: Yayi Xia
Writing – original draft: Chenhui Yang
Writing – review & editing: Yayi Xia
All authors reviewed and approved the final manuscript.

Ethics approval and consent to participate

All animal experiments were approved by the Institutional Animal Care and Use Committee (IACUC) of Lanzhou University Second Hospital (D2025-365) and conducted

in accordance with local guidelines for the care and use of laboratory animals.

Consent for publication

Not applicable

Availability of data

Data is available from the corresponding author upon reasonable request.

References

1. Xu J, Ji J, Jiao J, *et al*. 3D printing for bone-cartilage interface regeneration. *Front Bioeng Biotechnol*. 2022;10:828921. doi: 10.3389/fbioe.2022.828921
2. Jahani A, Nourbakhsh MS, Ebrahimzadeh MH, Mohammadi M, Yari D, PhD AM. Available 3D-printed biomolecule-loaded alginate-based scaffolds for cartilage tissue engineering applications: a review on current status and future prospective. *Arch Bone Jt Surg*. 2024;12(2):92-101. doi: 10.22038/abjs.2023.73275.3396
3. Liang Q, Ma Y, Yao X, Wei W. Advanced 3D-printing bioinks for articular cartilage repair. *IJB*. 2022;8(3):511. doi: 10.18063/ijb.v8i3.511
4. Deptuła M, Zawrzykraj M, Sawicka J, Banach-Kopeć A, Tylingo R, Pikuła M. Application of 3D-printed hydrogels in wound healing and regenerative medicine. *Biomed Pharmacother*. 2023;167:115416. doi: 10.1016/j.biopha.2023.115416
5. Nabizadeh Z, Nasrollahzadeh M, Daemi H, *et al*. Micro- and nanotechnology in biomedical engineering for cartilage tissue regeneration in osteoarthritis. *Beilstein J Nanotechnol*. 2022;13:363-389. doi: 10.3762/bjnano.13.31
6. Messaoudi O, Henrionnet C, Bourge K, Loeuille D, Gillet P, Pinzano A. Stem cells and extrusion 3D printing for Hyaline cartilage engineering. *Cells*. 2020;10(1):2. doi: 10.3390/cells10010002
7. Wei W, Ma Y, Yao X, *et al*. Advanced hydrogels for the repair of cartilage defects and regeneration. *Bioact Mater*. 2021;6(4):998-1011. doi: 10.1016/j.bioactmat.2020.09.030
8. Zhang W, Chen R, Xu X, *et al*. Construction of biocompatible hydrogel scaffolds with a long-term drug release for facilitating cartilage repair. *Front Pharmacol*. 2022;13:922032. doi: 10.3389/fphar.2022.922032
9. Liu Y, Peng L, Li L, *et al*. 3D-bioprinted BMSC-laden biomimetic multiphasic scaffolds for efficient repair of osteochondral defects in an osteoarthritic rat model. *Biomaterials*. 2021;279:121216. doi: 10.1016/j.biomaterials.2021.121216
10. Chen X, Wang Y, Chen R, Qu N, Zhang B, Xia C. Suppressing PLCγ1 enhances osteogenic and chondrogenic potential of BMSCs. *Biochem Biophys Res Commun*. 2020;532(2):292-299. doi: 10.1016/j.bbrc.2020.08.049
11. Xu Y, Wang Y, Wang A, *et al*. Effect of CD44 on differentiation of human amniotic mesenchymal stem cells into chondrocytes via Smad and ERK signaling pathways. *Mol Med Rep*. 2020;21(4):1777-1786. doi: 10.3892/mmr.2020.11044
12. Hou M, Zhang Y, Zhou X, *et al*. Kartogenin prevents cartilage degradation and alleviates osteoarthritis progression in mice via the miR-146a/NRF2 axis. *Cell Death Dis*. 2021;12(5):503. doi: 10.1038/s41419-021-03765-x
13. Wang J, Zhou J, Zhang N, Zhang X, Li Q. A heterocyclic molecule kartogenin induces collagen synthesis of human dermal fibroblasts by activating the smad4/smad5 pathway. *Biochem Biophys Res Commun*. 2014;450(1):568-574. doi: 10.1016/j.bbrc.2014.06.016
14. de Kroon LMG, Narcisi R, van den Akker GGH, *et al*. SMAD3 and SMAD4 have a more dominant role than SMAD2 in TGFβ-induced chondrogenic differentiation of bone marrow-derived mesenchymal stem cells. *Sci Rep*. 2017;7(1):43164. doi: 10.1038/srep43164
15. Pu P, Wu S, Zhang K, *et al*. Mechanical force induces macrophage-derived exosomal UCHL3 promoting bone marrow mesenchymal stem cell osteogenesis by targeting SMAD1. *J Nanobiotechnol*. 2023;21(1):180. doi: 10.1186/s12951-023-01836-z
16. Zhang S, Hu P, Liu T, *et al*. Kartogenin hydrolysis product 4-aminobiphenyl distributes to cartilage and mediates cartilage regeneration. *Theranostics*. 2019;9(24):7108-7121. doi: 10.7150/thno.38182
17. Dey MK, Devireddy RV. Rheological characterization and printability of sodium alginate–gelatin hydrogel for 3D cultures and bioprinting. *Biomimetics*. 2025;10(1):28. doi: 10.3390/biomimetics10010028
18. Yu PB, Deng DY, Lai CS, *et al*. BMP type I receptor inhibition reduces heterotopic ossification. *Nat Med*. 2008;14(12):1363-1369. doi: 10.1038/nm.1888
19. Tsukamoto S, Mizuta T, Fujimoto M, *et al*. Smad9 is a new type of transcriptional regulator in bone morphogenetic protein signaling. *Sci Rep*. 2014;4:7596. doi: 10.1038/srep07596
20. Yao Y, Wei G, Deng L, Cui W. Visualizable and lubricating hydrogel microspheres via NanoPOSS for cartilage regeneration. *Adv Sci (Weinh)*. 2023;10(15):e2207438. doi: 10.1002/advs.202207438
21. Chen Y, Yan X, Yuan F, *et al*. Kartogenin-conjugated double-network hydrogel combined with stem cell transplantation

and tracing for cartilage repair. *Adv Sci (Weinh)*. 2022;9(35):e2105571.
doi: 10.1002/advs.202105571

22. Xu T, Yu X, Xu K, *et al*. Comparison of the ability of exosomes and ectosomes derived from adipose-derived stromal cells to promote cartilage regeneration in a rat osteochondral defect model. *Stem Cell Res Ther*. 2024;15(1):1.
doi: 10.1186/s13287-024-03632-4

23. Wang M, Wu Y, Li G, *et al*. Articular cartilage repair biomaterials: strategies and applications. *Mater Today Bio*. 2024;24:100948.
doi: 10.1016/j.mtbio.2024.100948

24. Wu Z, Yao H, Sun H, *et al*. Enhanced hyaline cartilage formation and continuous osteochondral regeneration via 3D-Printed heterogeneous hydrogel with multi-crosslinking inks. *Mater Today Bio*. 2024;26:101080.
doi: 10.1016/j.mtbio.2024.101080

25. Mikaeeli Kangarshahi B, Naghib SM, Rabiee N. 3D printing and computer-aided design techniques for drug delivery scaffolds in tissue engineering. *Expert Opin Drug Deliv*. 2024;21(11):1615-1636.
doi: 10.1080/17425247.2024.2409913

26. Hafezi M, Nouri Khorasani S, Zare M, Esmaeely Neisiany R, Davoodi P. Advanced hydrogels for cartilage tissue engineering: recent progress and future directions. *Polymers (Basel)*. 2021;13(23):4199.
doi: 10.3390/polym13234199

27. Antich C, de Vicente J, Jiménez G, *et al*. Bio-inspired hydrogel composed of hyaluronic acid and alginate as a potential bioink for 3D bioprinting of articular cartilage engineering constructs. *Acta Biomater*. 2020;106:114-123.
doi: 10.1016/j.actbio.2020.01.046

28. Murphy CA, Serafin A, Collins MN. Development of 3D printable gelatin methacryloyl/chondroitin sulfate/hyaluronic acid hydrogels as implantable scaffolds. *Polymers (Basel)*. 2024;16(14):1958.
doi: 10.3390/polym16141958

29. Dai W, Zhang L, Yu Y, *et al*. 3D bioprinting of heterogeneous constructs providing tissue-specific microenvironment based on host–guest modulated dynamic hydrogel bioink for osteochondral regeneration. *Adv Funct Mater*. 2022;32(23):2200710.
doi: 10.1002/adfm.202200710

30. Zhang Y, Li D, Liu Y, *et al*. 3D-bioprinted anisotropic bicellular living hydrogels boost osteochondral regeneration via reconstruction of cartilage–bone interface. *Innovation (Camb)*. 2024;5(1):100542.
doi: 10.1016/j.xinn.2023.100542

31. Song C, Wu X, Wei Z, Xu Y, Wang Y, Zhao Y. Dental pulp stem cells-loaded kartogenin-modified hydrogel microspheres with chondrocyte differentiation property for cartilage repair. *Chem Eng J*. 2024;496:153930.
doi: 10.1016/j.cej.2024.153930

32. Yan H, Yu T, Li J, *et al*. Kartogenin improves osteogenesis of bone marrow mesenchymal stem cells via autophagy. *Stem Cells Int*. 2022;2022:1278921.
doi: 10.1155/2022/1278921

33. Li TF. TGF-b signaling in chondrocytes. *Front Biosci*. 2005;10(1-3):681-685.
doi: 10.2741/1563

34. Li J, Dong S. The signaling pathways involved in chondrocyte differentiation and hypertrophic differentiation. *Stem Cells Int*. 2016;2016:2470351.
doi: 10.1155/2016/2470351

35. Huntley R, Jensen E, Gopalakrishnan R, Mansky KC. Bone morphogenetic proteins: their role in regulating osteoclast differentiation. *Bone Rep*. 2019;10:100207.
doi: 10.1016/j.bonr.2019.100207

36. Lu C, Dong X, Yu WP, *et al*. Inorganic phosphate-osteogenic induction medium promotes osteogenic differentiation of valvular interstitial cells via the BMP-2/Smad1/5/9 and RhoA/ROCK-1 signaling pathways. *Am J Transl Res*. 2020;12(7):3329-3345.

37. Wang T, Zhang C, Wu C, *et al*. miR-765 inhibits the osteogenic differentiation of human bone marrow mesenchymal stem cells by targeting BMP6 via regulating the BMP6/Smad1/5/9 signaling pathway. *Stem Cell Res Ther*. 2020;11(1):251.
doi: 10.1186/s13287-020-1579-0

38. Ampuja M, Kallioniemi A. Transcription factors—intricate players of the bone morphogenetic protein signaling pathway. *Genes Chromosomes Cancer*. 2017;57(1):3-11.
doi: 10.1002/gcc.22502